

The total mass of the Large Magellanic Cloud from its perturbation on the Orphan stream

D. Erkal,^{1*} V. Belokurov,^{2,3} C. F. P. Laporte,⁴ S. E. Koposov,^{5,2} T. S. Li,^{6,7} C. J. Grillmair,⁸ N. Kallivayalil,⁹ A. M. Price-Whelan,¹⁰ N. W. Evans,² K. Hawkins,¹¹ D. Hendel,¹² C. Mateu,¹³ J. F. Navarro,¹⁴ A. del Pino,¹⁵ C. T. Slater,¹⁶ and S. T. Sohn¹⁵

(The OATs: Orphan Aspen Treasury Collaboration)

¹ Department of Physics, University of Surrey, Guildford GU2 7XH, UK

² Institute of Astronomy, University of Cambridge, Madingley Road, Cambridge CB3 0HA, UK

³ Center for Computational Astrophysics, Flatiron Institute, 162 5th Avenue, New York, NY 10010, USA

⁴ CITA National Fellow, Department of Physics and Astronomy, University of Victoria, 3800 Finnerty Road, Victoria, BC, V8P 5C2, Canada

⁵ Carnegie Mellon University, 5000 Forbes Ave, Pittsburgh, PA, 15213, USA

⁶ Fermi National Accelerator Laboratory, P.O. Box 500, Batavia, IL 60510, USA

⁷ Kavli Institute for Cosmological Physics, University of Chicago, Chicago, IL 60637, USA

⁸ IPAC, Mail Code 314-6, Caltech, 1200 E. California Blvd., Pasadena, CA 91125, USA

⁹ Department of Astronomy, University of Virginia, 530 McCormick Road, Charlottesville, VA 22904, USA

¹⁰ Department of Astrophysical Sciences, Princeton University, 4 Ivy Lane, Princeton, NJ 08544, USA

¹¹ Department of Astronomy, The University of Texas at Austin, 2515 Speedway Boulevard, Austin, TX 78712, USA

¹² Department of Astronomy and Astrophysics, University of Toronto, 50 St. George Street, Toronto, Ontario, M5S 3H4, Canada

¹³ Departamento de Astronomía, Instituto de Física, Universidad de la República, Iguá 4225, CP 11400 Montevideo, Uruguay

¹⁴ Senior CIFAR Fellow, Department of Physics and Astronomy, University of Victoria, 3800 Finnerty Road, Victoria, BC, V8P 5C2 Canada

¹⁵ Space Telescope Science Institute, 3700 San Martin Drive, Baltimore 21218, USA

¹⁶ Department of Astronomy, University of Washington, Box 351580, Seattle, WA 98195, USA

16 May 2019

ABSTRACT

In a companion paper by Koposov et al., RR Lyrae from *Gaia* Data Release 2 are used to demonstrate that stars in the Orphan stream have velocity vectors significantly misaligned with the stream track, suggesting that it has received a large gravitational perturbation from a satellite of the Milky Way. We argue that such a mismatch cannot arise due to any realistic static Milky Way potential and then explore the perturbative effects of the Large Magellanic Cloud (LMC). We find that the LMC can produce precisely the observed motion-track mismatch and we therefore use the Orphan stream to measure the mass of the Cloud. We simultaneously fit the Milky Way and LMC potentials and infer that a total LMC mass of $1.38^{+0.27}_{-0.24} \times 10^{11} M_{\odot}$ is required to bend the Orphan Stream, showing for the first time that the LMC has a large and measurable effect on structures orbiting the Milky Way. This has far-reaching consequences for any technique which assumes that tracers are orbiting a static Milky Way. Furthermore, we measure the Milky Way mass within 50 kpc to be $3.80^{+0.14}_{-0.11} \times 10^{11} M_{\odot}$. Finally, we use these results to predict that, due to the reflex motion of the Milky Way in response to the LMC, the outskirts of the Milky Way's stellar halo should exhibit a bulk, upwards motion.

Key words: Galaxy: kinematics and dynamics, Galaxy: halo, Galaxy: structure, Galaxy: evolution, galaxies: Magellanic Clouds

1 INTRODUCTION

The total mass of a galaxy is hard to measure (White 2001). While it can be done in a statistical sense for a sample of objects using,

for example, weak lensing (see e.g. Mandelbaum et al. 2006) or halo abundance matching (e.g. Moster, Naab & White 2013), for individual galaxies, the total mass is always an extrapolation. For high-luminosity galaxies, a variety of galaxy-weighting methods exist which rely on either the availability of kinematic tracers (e.g. Wilkinson & Evans 1999; Cappellari et al. 2006; Xue et al. 2008)

* d.erkal@surrey.ac.uk

or the presence of a gravitational lensing signal (e.g. Kochanek, Keeton & McLeod 2001), or both (e.g. Sand, Treu & Ellis 2002; Treu & Koopmans 2004; Auger et al. 2010).

In all cases, the measurement is limited by the extent of the kinematic tracers which rarely reach out to a substantial fraction of the virial radius. For dwarf galaxies, the uncertainty related to the extrapolation of the mass probed to the virial radius is exacerbated by the absence of tracers at intermediate and large distances (e.g. Aaronson 1983; Kleyna et al. 2005; Walker et al. 2009; Agnello & Evans 2012; Errani, Peñarrubia & Walker 2018).

Stellar streams have recently been demonstrated to provide a new and independent method to gauge the mass distribution inside our own Milky Way (see e.g. Johnston et al. 1999; Koposov, Rix & Hogg 2010; Gibbons, Belokurov & Evans 2014; Küpper et al. 2015) and a handful of nearby galaxies (e.g. Ibata et al. 2004; Fardal et al. 2013; Amorisco, Martínez-Delgado & Schedler 2015). Tidal streams not only measure the mass within the extent of the stream, but also provide constraints on the slope of the total matter density (see Gibbons, Belokurov & Evans 2014), thus allowing us to pin down the host’s mass further out (see also Bonaca & Hogg 2018). Moreover, streams are sensitive probes of the shape of the underlying potential (see Ibata et al. 2001; Helmi 2004; Johnston, Law & Majewski 2005; Fellhauer et al. 2006; Law & Majewski 2010; Bowden, Belokurov & Evans 2015) and their twisting and fanning can be used to understand the amount of asphericity of the Dark Matter halo (see Pearson et al. 2015; Erkal, Sanders & Belokurov 2016).

As numerous examples of halo substructure started to be discovered in the Milky Way, perturbations of stellar streams were put forward as a new promising diagnostic, capable of constraining masses of Galactic satellites, even those entirely devoid of light (see e.g. Ibata et al. 2002; Johnston, Spergel & Haydn 2002; Siegal-Gaskins & Valluri 2008; Carlberg 2009; Yoon, Johnston & Hogg 2011; Ngan & Carlberg 2014; Erkal & Belokurov 2015). Such perturbations arise as a result of the stream-subhalo interaction during which the paths of the stars around the point of the closest approach are slightly altered after receiving a velocity kick from the passing deflector. The affected stars begin to re-arrange their orbits, and, with time, small differences can accumulate to produce observable signatures (e.g. Carlberg, Grillmair & Hetherington 2012; Carlberg & Grillmair 2013; Bovy, Erkal & Sanders 2017; Erkal, Koposov & Belokurov 2017; de Boer et al. 2018; Price-Whelan & Bonaca 2018). However, when the perturbation is strong enough, its effect on the stream can be spotted soon after the interaction. For fast encounters with dense objects, this can eject stars from the stream and lead to spur-like features (e.g., Bonaca et al. 2018). If the perturber is very massive and less dense, the kick received by the stars can be large enough to cause the stream’s velocity vector to become misaligned with the original direction of the stream’s motion (Erkal et al. 2018).

With a stellar mass of $2.7 \times 10^9 M_{\odot}$ (van der Marel 2006), the LMC is our Galaxy’s largest satellite and thus is certainly capable of causing detectable perturbations in some of the Milky Way stellar streams. The number of streams affected, and the strength of the effect, depends on the total mass of the Cloud and its distance. While the latter is well known (~ 50 kpc, Pietrzyński et al. 2013), the former is currently not constrained. Efforts to measure the Cloud’s mass directly from the dynamics of the LMC clusters (Schommer et al. 1992) or via modelling of its rotation curve (van der Marel & Kallivayalil 2014) have both given relatively modest estimates of $\sim 2 \times 10^{10} M_{\odot}$ within ~ 9 kpc. However, wide-field surveys have recently revealed a wealth of debris in the outskirts of

the LMC (e.g. Mackey et al. 2016; Besla et al. 2016; Belokurov & Koposov 2016; Deason et al. 2017; Belokurov et al. 2017; Mackey et al. 2018; Navarrete et al. 2019; Choi et al. 2018; Nidever et al. 2019), indicating that the Cloud may be significantly more massive. Indeed, several distinct lines of reasoning have suggested an LMC mass of $\sim 1\text{--}2.5 \times 10^{11} M_{\odot}$. First, requiring that the LMC and SMC are bound together requires an LMC mass above $\sim 10^{11} M_{\odot}$ (Kallivayalil et al. 2013). Second, accounting for the LMC in the timing argument between the Milky Way and M31, as well as in the nearby Hubble flow, gives an LMC mass of $2.5 \times 10^{11} M_{\odot}$ (Peñarrubia et al. 2016). Third, live N-body models of the LMC on a first infall orbit (Laporte et al. 2018) favor a massive LMC of $2.5 \times 10^{11} M_{\odot}$ to explain the shape of the HI warp (Levine, Blitz & Heiles 2006) through the response of the halo (Weinberg 1998). Finally, abundance matching (Moster, Naab & White 2013; Behroozi, Wechsler & Conroy 2013) based on the LMC’s stellar mass of $2.7 \times 10^9 M_{\odot}$ (van der Marel 2006) gives a peak halo mass of $2 \times 10^{11} M_{\odot}$. These results suggest that the LMC’s diminutive size on the sky belies its true mass.

The influence of the LMC on the behavior of stellar streams around the Milky Way was originally considered in Law & Majewski (2010) who discussed the interaction of a relatively light Cloud ($< 6 \times 10^{10} M_{\odot}$) with the Sagittarius stream and found that it could have a significant effect. Vera-Ciro & Helmi (2013) followed this up and argued that including a $8 \times 10^{10} M_{\odot}$ LMC could change the Milky Way halo shape inferred by Law & Majewski (2010), making it more spherical. Along these lines, Gómez et al. (2015) simulated the infall of a $1.8 \times 10^{11} M_{\odot}$ LMC and found that it would induce a significant reflex motion in the Milky Way which would affect the Sagittarius stream. More recently, Erkal et al. (2018) studied the effect of the LMC on the Tucana III stream and found that it could induce a substantial proper motion perpendicular to the stream which would be detectable in *Gaia* DR2. They further argued that the size of this offset could be used to measure the mass of the LMC.

Here we present the results of a comprehensive modeling of the Orphan Stream (OS, Grillmair 2006; Belokurov et al. 2007), inspired by its recent detection in the *Gaia* data presented in Koposov et al. (2019). In the *Gaia* Data Release 2 (see *Gaia* Collaboration et al. 2018), RR Lyrae stars have been used to trace the OS over $> 200^{\circ}$ on the sky, revealing the details of its behavior in 5 out of 6 dimensions of the phase-space, i.e. on-sky position, distance, and proper motions. The stream’s track is shown to swing by some 20° when the 3D positions of its Southern members are compared to those in the North. Moreover, across tens of degrees, the proper motions of the OS’s RR Lyrae are demonstrably offset from the direction delineated by the stream’s extent. We propose that the large-scale wobble of the Orphan’s track together with the stream-proper motion misalignment reported in Koposov et al. (2019) are best explained as a result of an interaction between the stream and the LMC. We explore a range of Milky Way mass models and allow for the Galaxy’s Dark Matter halo to be aspherical with the flattened axis oriented in an arbitrary direction. We also include the effects of the Milky Way’s response to the LMC’s infall (see e.g. Gómez et al. 2015).

This paper is organized as follows. In Section 2 we present the observed misalignment in the Orphan stream with a new technique. In Section 3 we attempt to fit the Orphan stream in the presence of just the Milky Way and show that even with a flexible potential, it is not possible to get a good match. Next, we perform the same fits including the LMC in Section 4 which can reproduce the Orphan stream. These fits constrain the LMC mass and the shape of the

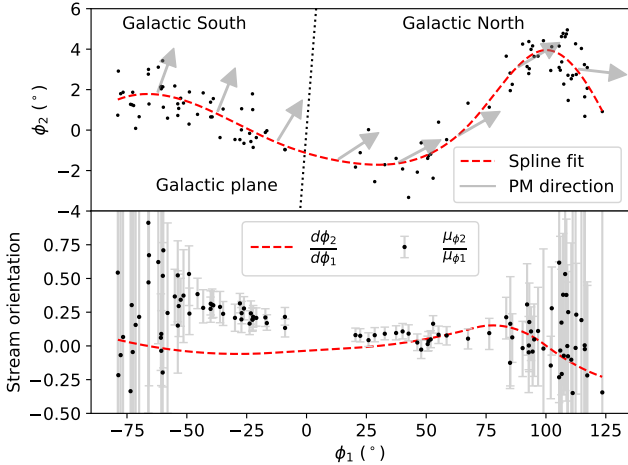


Figure 1. Stream track and ratio of proper motions showing misalignment in the Orphan stream. **Top panel** shows the Orphan stream in coordinates aligned with the stream. The black points are RR Lyrae from [Koposov et al. \(2019\)](#), the dashed-red line shows a cubic spline fit to these points, and the dotted line shows the galactic plane. The grey arrows show the reflex-corrected proper motion direction at 25° intervals along the stream. In a stream orbiting a static, non-interacting Milky Way, these arrows would be expected to point along the stream. Note that the final proper motion direction at $\phi_1 \sim 110^\circ$ has a large uncertainty and thus its misalignment is not significant. **Lower panel:** Ratio of the reflex corrected proper motions along the stream (black point with grey bars) and the slope of the stream (dashed-red curve). There is a mismatch for $\phi_1 < 50^\circ$ where the stream track has a negative slope but the proper motions indicate a positive slope. This mismatch is the strongest below $\phi_1 \sim 0^\circ$ which corresponds to the Southern Galactic hemisphere.

Milky Way halo. We discuss the meaning and implications of these results in Section 5 before concluding in Section 6.

2 MISALIGNED ORPHAN STREAM

Streams can be shown to approximately delineate orbits ([Sanders & Binney 2013](#)), which implies that the constituent stars move mostly along the stream. Indeed, this near-alignment has been proposed as a way to measure the velocity of the Sun ([Majewski et al. 2006](#); [Malhan & Ibata 2017](#); [Hayes, Law & Majewski 2018](#)) and, naturally, as a means of finding streams ([Malhan & Ibata 2018](#)). In order to see how this motion along the stream relates the debris path and its proper motion, let us consider a stream in an on-sky coordinate system where it follows a track $(\phi_1(s), \phi_2(s))$ parameterized by s . If the proper motions are aligned with the stream track, then the tangent to the stream, $(\frac{d\phi_1}{ds}, \frac{d\phi_2}{ds})$, should be proportional to the motion of the stars along the stream, $(\frac{d\phi_1}{dt}, \frac{d\phi_2}{dt}) = (\mu_{\phi_1}, \mu_{\phi_2})$. Note that we assume that the proper motions are corrected for the Solar reflex. We emphasize that μ_{ϕ_1} is the proper motion in ϕ_1 without the traditional $\cos(\phi_2)$ correction. In practice, we compare the slope of the stream on the sky, $\frac{d\phi_2}{d\phi_1}$, to the ratio of the proper motions in the stream, $\frac{\mu_{\phi_2}}{\mu_{\phi_1}}$. Replacing $\phi_2(s)$ with the distance to the stream, $r(s)$, this argument also implies that $\frac{v_r}{\mu_{\phi_1}}$ can be compared with $\frac{dr}{d\phi_1}$ where v_r is the Solar reflex corrected radial velocity, i.e. v_{gsr} . Note that these comparisons can be made in any coordinates and can be used to easily determine whether the stream has been significantly perturbed.

Observationally, the motion-track alignment has been demonstrated in several streams in the Milky Way. For example, both the GD-1 ([Grillmair & Dionatos 2006](#)) and the Palomar 5 streams ([Odenkirchen et al. 2001](#)) have proper motions closely aligned with their stream tracks ([Koposov, Rix & Hogg 2010](#); [Fritz & Kallivayalil 2015](#), respectively).

In Figure 1 we investigate whether the assumption of motion-track alignment holds for the OS, as traced using RR Lyrae from *Gaia* DR2 (see [Koposov et al. 2019](#)). The (ϕ_1, ϕ_2) coordinates are obtained by a rotation of the celestial equator to a great circle with a pole of $(\alpha_{\text{pole}}, \delta_{\text{pole}}) = (72^\circ, -14^\circ)$ and a zero point at $(\alpha, \delta) = (191.10487^\circ, 62.86084^\circ)$. The top panel shows the RR Lyrae on the sky along with a cubic spline fit (dashed-red curve). The cubic spline uses fixed nodes with a spacing of 30° . The bottom panel shows the slope of this track (dashed-red curve) along with the ratio of the reflex-corrected proper motions (black points with grey error bars). The error bars come from Monte Carlo sampling of the proper motions and the distances given the observational uncertainties. The errors are largest at the ends of the visible stream due to their relatively large distances ($r > 30$ kpc).

The stream track and proper motions are misaligned for $\phi_1 < 50^\circ$ with the strongest mismatch below $\phi_1 < 0^\circ$. Interestingly, this corresponds to the previously unseen portion of Orphan in the Southern Galactic hemisphere where the stream is closest to the LMC. To give a sense of the magnitude of the misalignment, in the top panel light grey arrows show the proper motion direction averaged in 25° intervals along the stream. There is a clear misalignment in the South where the proper motions point upwards but the stream has a gentle negative slope. Note that the top panel of Figure 1 slightly exaggerates the misalignment due to the aspect ratio of the figure.

3 FITTING THE NORTHERN PART OF THE STREAM

Given the strong misalignment seen in Figure 1, it is clear that orbit modelling will fail for this particular stream since the orbit's projection on the sky and its proper motion are always aligned by construction. Therefore, in what follows we instead use realistic stream models. We start by fitting only the Northern portion of the OS in a Galaxy model with an aspherical Dark Matter halo. This allows us to both compare to the results in the literature (although a genuine stream model has not yet been used to explain even the Northern data) and to better elucidate the effect of the LMC. We then demonstrate how different mass LMCs can deflect the Southern portion of such a model stream and effortlessly bring it into agreement with the Orphan data. Later, in Section 4, we will explore models of the entire stream.

3.1 Setup

We generate streams using the modified Lagrange Cloud Stripping (mLCS) technique developed in [Gibbons, Belokurov & Evans \(2014\)](#). This method rapidly generates streams by ejecting swarms of test particles from the Lagrange points of a progenitor whose gravitational potential is represented analytically. We model the Orphan's progenitor as a $10^7 M_\odot$ (in approximate agreement with the observationally-motivated mass estimates from [Koposov et al. 2019](#)) Plummer sphere with a scale radius of 1 kpc. These parameters were chosen to roughly match the width of the OS. For the Milky Way gravitational potential, we choose a generalized version of `MWPotential2014` from [Bovy \(2015\)](#) which consists of an

NFW halo (Navarro, Frenk & White 1997), a Miyamoto-Nagai disk (Miyamoto & Nagai 1975), and a power-law bulge with an exponential cutoff. We parameterize the NFW halo in terms of its mass, M_{NFW} , a scale radius, $r_{s,\text{NFW}}$, and a fixed concentration $c = 15.3$. The Miyamoto-Nagai disk has a mass of $6.8 \times 10^{10} M_{\odot}$, a scale radius of 3 kpc, and a scale height of 280 pc. For simplicity, we replace the bulge with a Hernquist profile (Hernquist 1990) with the same mass ($5 \times 10^9 M_{\odot}$) and a scale radius of 500 pc. For the fits, we keep the disk and bulge fixed but allow the mass of the NFW halo to vary. We introduce a flattening in the halo potential by writing the NFW potential as

$$\phi_{\text{NFW}}(x, y, z) = -\frac{GM_{\text{NFW}}}{\tilde{r}} \frac{\log(1 + \frac{\tilde{r}}{r_s})}{\log(1+c) - \frac{c}{1+c}}, \quad (1)$$

where M_{NFW} , r_s , and c are the NFW halo's mass, scale radius, and concentration respectively, while

$$\tilde{r}^2 = x^2 + y^2 + z^2 + \left(\frac{1}{q^2} - 1\right)(\hat{\mathbf{n}} \cdot \mathbf{x})^2, \quad (2)$$

$\hat{\mathbf{n}}$ is the unit vector in which the potential is flattened by q , and $\mathbf{x} = (x, y, z)$. For $\hat{\mathbf{n}}$ pointed in the z direction, this reduces to the commonly used form (e.g. Richstone 1980; Evans 1994). Note that that our potential (1) has the advantage that the force components are analytic, thus speeding our computations. However, it has the disadvantage that the density is not everywhere positive (unless $q = 1$). This defect normally occurs at radii well beyond the regime relevant for our simulations. It is also worth bearing in mind that the density contours can deviate substantially from an ellipsoidal shape, so q is best interpreted as a diagnostic of the effect of the LMC on the OS orbit rather than the intrinsic flattening of the Milky Way halo. We will discuss this interpretation further in Section 5.3.

We take the Sun's velocity relative to the Galactic standard of rest to be (11.1, 245, 7.3) km/s. The y component of this velocity is based on the proper motion of Sgr A* (Reid & Brunthaler 2004) and the distance to the Galactic center of 8.1 kpc from Gravity Collaboration et al. (2018). The x and z components come from Schönrich, Binney & Dehnen (2010). We note that since the OS mostly probes the outer part of the Milky Way, we will keep these parameters fixed instead of relating the circular velocity at the Sun's location to the potential.

We fit the RR Lyrae from Koposov et al. (2019). These data are shown as black points in Figure 2. In order to clarify the effect of the LMC, in this Section we choose to only fit the stars with $\phi_1 > 50^\circ$. These are also the stars which do not show any significant proper motion offset (see Fig. 1) so we expect these have not been heavily perturbed by the LMC. This ϕ_1 range also corresponds to the portion of the stream with previously available data which were modelled in Newberg et al. (2010) and Hendel et al. (2018) so we can also compare our results to those in the literature. We note that for a sub-section of the stream, Koposov et al. (2019) also presented two additional debris track measurements, one based on Red Giant Branch (RGB) stars from *Gaia* DR2 and one computed using the RGB/Main Sequence Turn-Off stars in DECaLS (Dey et al. 2018). These tracks show good agreement overall, though a small offset near $\phi_1 \sim 100^\circ$ (see their Fig. 8) is reported. For the sake of consistency, we choose to only fit the GDR2 RR Lyrae (covering the entire detected length of the stream). We will discuss possible implications of our choice in Section 5. Koposov et al. (2019) also present radial velocities of Orphan stream stars from SDSS which we compare against our best-fit streams but we do not use in our fits.

Since the progenitor of the OS is not known (but see the dis-

ussion of a possible association between the OS and the Gru 2 satellite in Koposov et al. 2019), we should in principle include its position as a free parameter in our model. Indeed, in Section 4 we consider multiple progenitor positions and find that our results are independent of this choice. However, in this section we choose to place the progenitor at $\phi_1 = 50^\circ$ since we will only be fitting the RR Lyrae with $\phi_1 > 50^\circ$. This forces the progenitor to be on the stream so that we can later include the LMC and see how it deflects the stream. To describe the progenitor's present day position and velocity we then have 5 additional parameters: the two proper motions ($\mu_{\alpha,\text{prog}}^*, \mu_{\delta,\text{prog}}^*$), the radial velocity ($v_{r,\text{prog}}$), the distance (d_{prog}), and the latitude ($\phi_{2,\text{prog}}$). Once these parameters are specified, we then evolve the stream backwards for 5 Gyr and then use the mLCS technique to generate the stream's present configuration. We strip stars with a Gaussian spread of 100 Myr around each pericenter with respect to the Milky Way. In order to ensure that there are enough particles in the stream, we strip 5,000 stars per pericentric passage.

3.2 Likelihood

The likelihood of the set of RR Lyrae from Koposov et al. (2019) is computed as follows. For each star i , four components of its phase-space position m_i are modelled, namely: latitude ϕ_2 , heliocentric distance, and both proper motion components. As described above, in this section we only fit the RR Lyrae with $\phi_1 > 50^\circ$. For each RR Lyra and each observable, we fit a straight line to the $m(\phi_1)$ distribution of particles in the simulated stream within 2.5° in ϕ_1 of the RR Lyrae. This fit returns the maximum likelihood value of the observable at the location of the RR Lyra, $m_{i,\text{sim}}$, and the width of that observable, $\sigma_{i,\text{sim}}$. The log likelihood takes the form

$$\log \mathcal{L}_i = -\frac{1}{2} \log \left(2\pi(\sigma_{i,\text{obs}}^2 + \sigma_{i,\text{sim}}^2) \right) - \frac{1}{2} \frac{(m_{i,\text{obs}} - m_{i,\text{sim}})^2}{\sigma_{i,\text{obs}}^2 + \sigma_{i,\text{sim}}^2}, \quad (3)$$

where $\sigma_{i,\text{obs}}$ is the observed uncertainty for each RR Lyrae and $m_{i,\text{obs}}$ is the value of the observable for i th star. This is then summed over all of the RR Lyrae and all of the observables. Note that we ignore the covariance between the two proper motions in our likelihood. This is justified since the median of the absolute magnitude of the correlation is small, 0.22 for the entire sample. If we restrict to the range where the proper motion errors are small, $-50^\circ < \phi_1 < 75^\circ$, the median drops to 0.14.

3.3 MCMC setup

We perform the Markov Chain Monte Carlo using EMCEE (Foreman-Mackey et al. 2013). Our model has 10 free parameters: 5 that describe the 6d position of the OS progenitor, the mass and scale radius of the NFW halo (r_s, M_{NFW}), as well as its flattening (q_{NFW}) and the orientation of the major axis on the sky ($l_{\text{NFW}}, b_{\text{NFW}}$). We use uniform priors over a broad range for all of these variables which are listed in Table 1. We use 200 walkers for 1500 steps with a burn-in of 750 steps.

3.4 Stream fit in an aspherical Milky Way

With the setup now defined, we proceed to fit the OS. Before beginning the MCMC sampling, we use the downhill simplex method to find the best-fit stream. We randomly sample 100 points from our priors in Table 1 and find two distinct solutions. Namely, we find

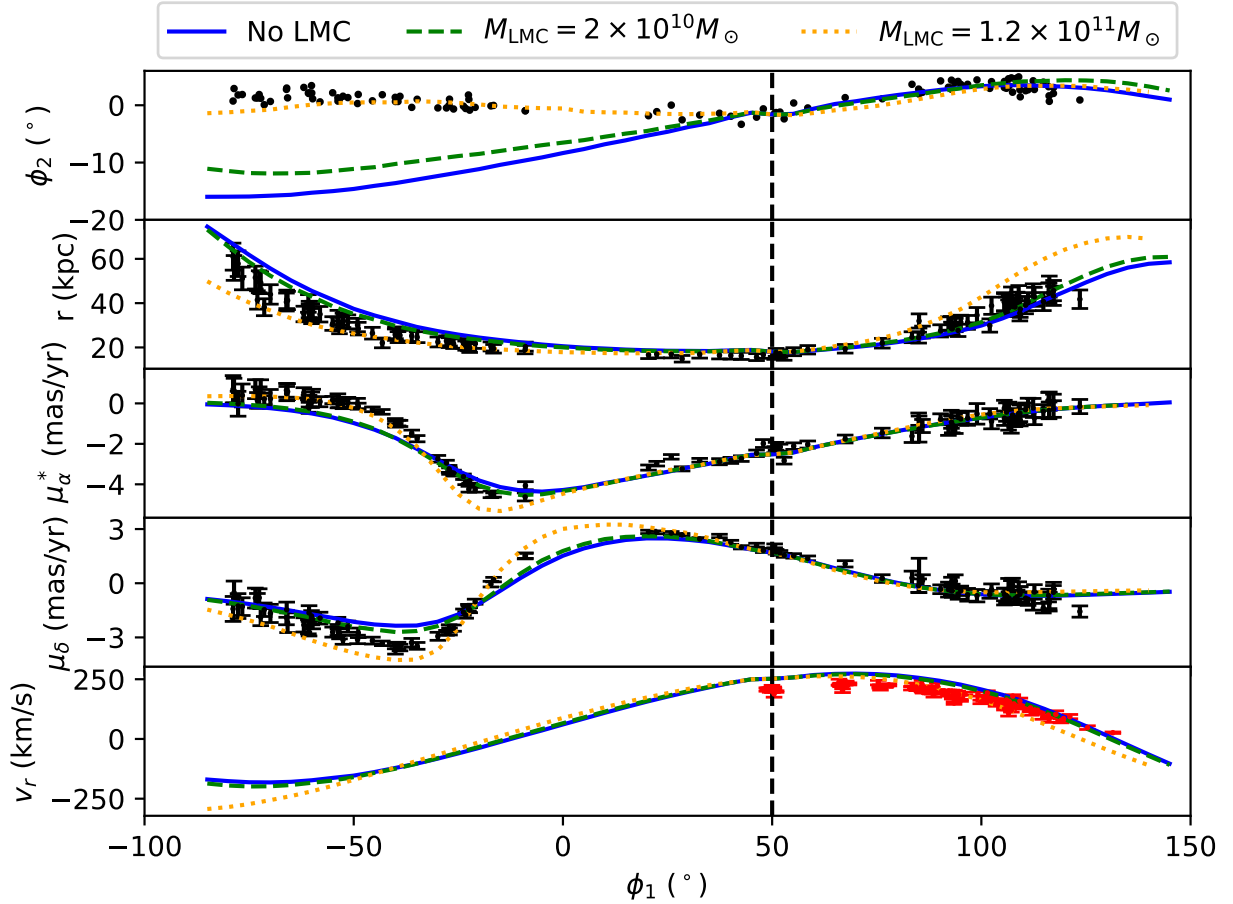


Figure 2. Best fit to the Northern portion of the OS in the Milky Way. From top to bottom the panels show the stream on the sky, the run of distances along the stream, the proper motion in RA, the proper motion in Dec, and the radial velocity. In the top four panels, the black points show the RR Lyrae from [Koposov et al. \(2019\)](#) and the red point shows an RR Lyrae which was removed from the fit since it appeared to be an outlier. The red points with error bars in the bottom panel show the radial velocities which are not used in the fit. The blue line shows the best-fit to the Northern portion of the OS ($\phi_1 > 50^\circ$, marked by the dotted line) in a Milky Way with an oblate halo. The dashed-green, dotted-orange lines show the same best-fit (i.e. same exact parameters) with a $2 \times 10^{10} M_\odot$, $1.2 \times 10^{11} M_\odot$ LMC respectively. This shows that the LMC should have a significant effect on the OS and that, at least in this simple case, a $1.2 \times 10^{11} M_\odot$ LMC broadly matches the observations. We stress that streams do not represent best-fits but rather are meant to showcase the effect of the LMC. Interestingly, it shows that the LMC also has a substantial effect on the Northern portion of the OS (e.g. large change in the distance) and thus fits to the Northern portion of the OS which neglect the LMC will likely be biased.

that both a prolate and an oblate halo (with different orientations) can fit the Northern part of the OS. We will return to these two solutions in Section 4 but in this section, for simplicity, we restrict the halo to be oblate.

The best-fit stream is shown with a blue curve in Figure 2. By design, this model provides a good fit to the Northern OS data, i.e. for stars with $\phi_1 > 50^\circ$. Outside of this range, the model matches reasonably well the distance and proper motions of the OS, but it shows a significant deviation in the track on the sky. The inability to simultaneously reproduce the proper motions and the stream track was foreshadowed in Figure 1 where we showed that the proper motions and the stream track had a pronounced offset. Note that we have also attempted to fit the entire range of the OS data in the presence of the Milky Way but we are unable to simultaneously match all observables (see next Section).

Interestingly, if we take this best-fit model from Figure 2 (i.e. the derived phase-space coordinates of the progenitor together with the potential parameters) and include a $2 \times 10^{10} M_\odot$ LMC (for the

details of the Cloud’s orbit see Section 4.1), we see that the predicted on-sky track (green dashed line) immediately swings much closer to the observed track. This shows that the LMC will have a substantial effect on the OS even if we limit its mass to that contained in its inner regions. If we then increase the LMC mass to $1.2 \times 10^{11} M_\odot$, we obtain a reasonable match to all of the stream’s observables (dotted orange line). This sensitivity suggests that the OS can be used to weigh the LMC. Let us stress that the dashed green line and the dotted orange line in Figure 2 are not independently derived models of the data. These phase-space tracks are obtained by taking the best-fit Milky Way-only model of the Northern portion of the OS and adding the LMC-like perturber on an appropriate orbit.

In order to compare our results with the work of [Newberg et al. \(2010\)](#) and [Hendel et al. \(2018\)](#) who performed orbit fits to Orphan, we compute the mass enclosed of the Milky Way within 60 kpc. Within this radius we measure a mass of $4.8 \pm 0.6 \times 10^{11} M_\odot$ where we have ignored the flattening of the halo. This mass matches

Parameter	Prior	Range
Orphan		
$\mu_{\alpha, \text{prog}}^*$	Uniform	(-6, 0) mas/yr
$\mu_{\delta, \text{prog}}$	Uniform	(0, 6) mas/yr
v_r, prog	Uniform	(-250, 250) km/s
d_{prog}	Uniform	(15, 20) kpc
$\phi_{2, \text{prog}}$	Uniform	(-10°, 10°)
Milky Way		
M_{NFW}	Uniform	$(6, 25) \times 10^{11} M_{\odot}$
r_s	Uniform	(10, 30) kpc
q_{NFW}	Uniform	(0.7, 1) or (1, 1.3)
l_{NFW}	Uniform	(0°, 360°)
b_{NFW}	Uniform	(-90°, 90°)
LMC		
M_{LMC}	Log-Uniform	$(10^8, 3 \times 10^{11}) M_{\odot}$
$\mu_{\alpha, \text{LMC}}^*$	Normal	1.91 ± 0.02 mas/yr
$\mu_{\delta, \text{LMC}}$	Normal	0.229 ± 0.047 mas/yr
v_r, LMC	Normal	262.2 ± 3.4 km/s
d_{LMC}	Normal	49.97 ± 1.126 kpc

Table 1. Priors for our MCMC fits. Note that the LMC priors are only used in the fits which include the LMC.

well with that of [Hendel et al. \(2018\)](#) who measured a mass of $5.6_{-1.2}^{+1.1} \times 10^{11} M_{\odot}$. However, it disagrees with the results of [Newberg et al. \(2010\)](#) who found a mass of $2.7 \times 10^{11} M_{\odot}$. Our result has an improved precision over previous results, expected given the quality of *Gaia* DR2.

Before proceeding to actually infer the LMC mass, we note that [Figure 2](#) also shows that while the OS is strongly deflected by the LMC in the South ($\phi_1 < 0^\circ$), it is also perturbed by it in the North. This is most evident in the distances and the stream track on the sky, as indicated by a noticeable deviation between the dotted orange line and the solid blue line at $\phi_1 > 50^\circ$. Thus, even if we only fit the OS data in the North, we would not recover the true Milky Way potential. Instead, the result of such a model would be biased since the potential would need to compensate for the influence of the LMC. Therefore, the effect of the LMC should be considered for all streams in the Milky Way when attempting to measure the potential.

4 FITTING THE ENTIRE STREAM

As argued in [Section 1](#), the LMC is the largest satellite of the Milky Way and is expected to have a substantial mass. Indeed, in [Section 3.4](#) we saw that including the LMC for the best-fit (of the Northern portion) of the OS in the Milky Way potential resulted in a large deflection of the stream. Interestingly, this deflection brought the Southern portion of Orphan into agreement with the data. In this section we will fit the entire OS data in the presence of the LMC and we will simultaneously constrain the LMC mass and the Milky Way halo.

4.1 Setup

The setup is very similar to that described in [Section 3.1](#) except that we now add in the LMC. For the LMC's present day position and velocity, we use proper motions of $\mu_{\alpha}^* = 1.91 \pm 0.02$ mas/yr, $\mu_{\delta} =$

0.229 ± 0.047 mas/yr ([Kallivayalil et al. 2013](#)), a radial velocity of $v_r = 262.2 \pm 3.4$ km/s ([van der Marel et al. 2002](#)), and a distance of 49.97 ± 1.126 kpc ([Pietrzyński et al. 2013](#)). The LMC is modeled as a Hernquist profile whose mass is left free. For each mass, we fix the scale radius so that the mass enclosed at 8.7 kpc matches the measured value of $1.7 \times 10^{10} M_{\odot}$ from [van der Marel & Kallivayalil \(2014\)](#). For LMC masses below $2 \times 10^{10} M_{\odot}$, we set the scale radius to 0.73 kpc. In order to correctly model the LMC's orbit around the Milky Way, we include dynamical friction following the results of [Jethwa, Erkal & Belokurov \(2016\)](#). We choose to place the OS progenitor at $\phi_1 = 6.34^\circ$ which is roughly half way between the two RR Lyrae closest to the origin. This choice is made to avoid having the progenitor within the observed portion of the stream. We also consider models where the progenitor is located at $\phi_1 = -90^\circ$ and $\phi_1 = 130^\circ$. However, since the results are independent of this choice we only show results for $\phi_1 = 6.34^\circ$.

When including the LMC, the stream generation proceeds almost identically to what is described in [Section 3.1](#) except that now the stream's progenitor is rewound and then disrupted in the combined presence of the Milky Way and the LMC. Our MCMC setup thus looks similar to the setup described in [Section 3.1](#) except that we have 5 additional parameters for the LMC: its mass, proper motions, radial velocity, and distance. The mass has a log-uniform prior between $10^8 - 3 \times 10^{11} M_{\odot}$ and the observables have Gaussian priors given from their measurements above. The proper motions, radial velocity, and distance have priors given by existing observations. [Table 1](#) contains a list of all the parameters and their priors.

Given that we now include the LMC, it is also natural to ask whether we should include the Small Magellanic Cloud (SMC). [Stanimirović, Staveley-Smith & Jones \(2004\)](#) measured the rotation curve of the SMC in HI and found a mass of $2.4 \times 10^9 M_{\odot}$ within 3 kpc. Since this is just the mass within a small aperture, the total pre-infall mass of the SMC was likely much higher. However, attempts to model the Magellanic stream seen in HI ([Putman et al. 2003](#)) have found that the SMC has likely had multiple pericentric passages with the LMC (e.g. [Besla et al. 2012](#)). Thus, the majority of its mass has likely been tidally stripped and is now orbiting the LMC. This is supported by i) the recent proper motion measurements within the SMC which suggest that the outer portions of the SMC are tidally disrupting ([Zivick et al. 2018](#)) and ii) the recent detection of the SMC's stellar tidal tails (see [Belokurov et al. 2017; Mackey et al. 2018; Belokurov & Erkal 2019](#)). Therefore, we choose to ignore the SMC in our analysis but note that a fraction of the mass we attribute to the LMC is due to the debris of the SMC.

4.2 Fitting Orphan in the presence of the LMC

The addition of the LMC to the model allows us to get a significantly better fit to the OS data than in the Milky Way alone. As discussed above, this is driven by the fact it is impossible to produce any considerable motion-track misalignment observed in the OS without including a massive perturber. Nonetheless, to ensure that our inference of the LMC mass is not biased by our choice of the Galaxy model we explore a generously wide range of Milky Way DM halo shapes. More precisely, when including the LMC, we consider three separate subsets of the Milky Way halo potential described in [Section 3.1](#): a spherical halo ($q_{\text{NFW}} = 1$), an oblate halo ($q_{\text{NFW}} < 1$), and a prolate halo ($q_{\text{NFW}} > 1$). The flattening direction of the halo is only included for non-spherical haloes. In addition to the halo shape, we also consider a Milky Way which is static and one which can respond to the LMC's infall. This is important since

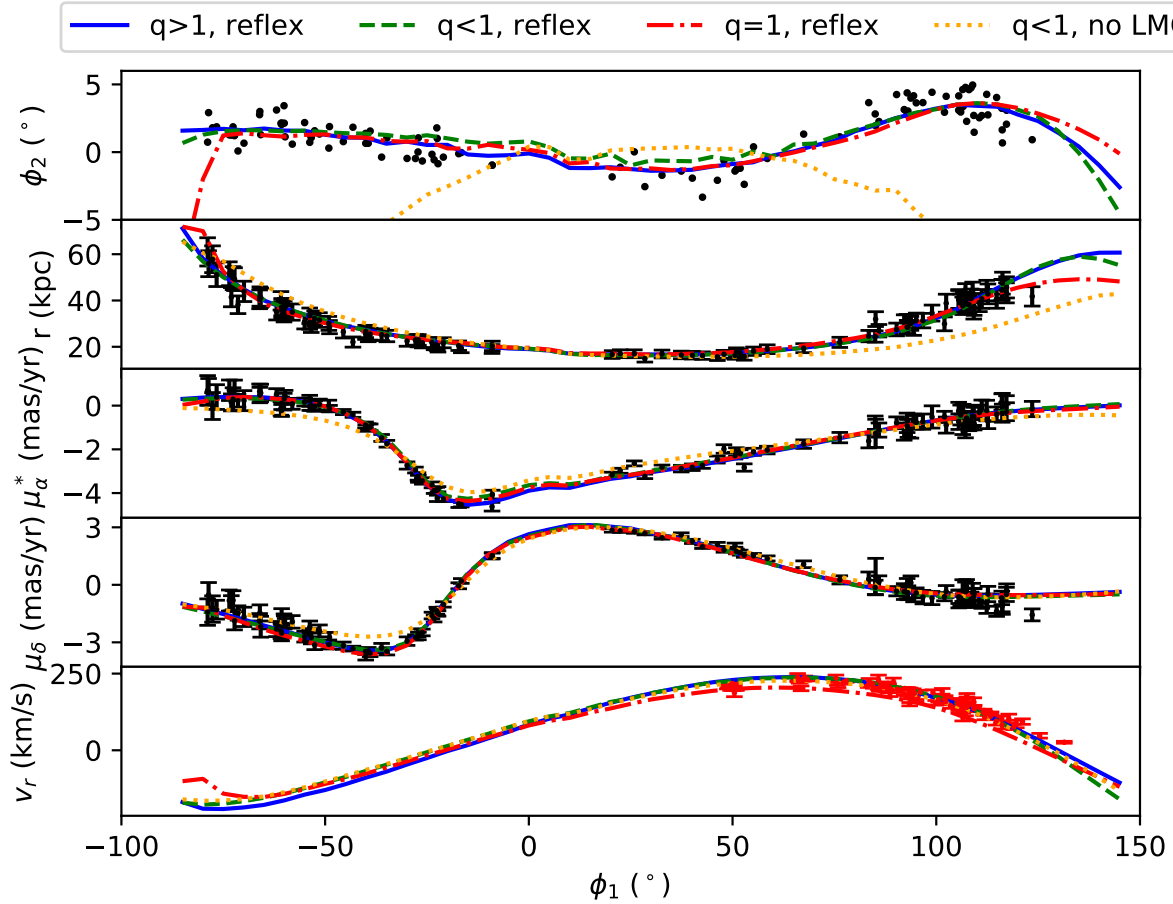


Figure 3. Comparison of the best fit models when fitting all of the RR Lyrae. The black points in the top four panels show the observed RR Lyrae from Koposov et al. (2019). The red points with error bars in the bottom panel show radial velocities from SDSS which are not included in the fit. The curves show the tracks of the best-fit streams in a prolate halo including the LMC (solid blue line) and a spherical halo including the LMC (dashed green line). In both these cases, the Milky Way halo is represented by a particle which can respond to the LMC. For comparison, a best-fit in an oblate halo without the LMC is included. While this can roughly match most of the observables, it fails to reproduce the stream track on the sky.

if the LMC is massive enough, it will induce a substantial reflex motion in the Milky Way (Weinberg 1989; Gómez et al. 2015). In order to account for this shift in the center of mass, we treat the Milky Way as a movable particle that sources a potential. We give the results of these six fits in Table 2. In general we find that the fits in a reflexive Milky Way halo are best for each choice of the halo shape and consequently, throughout the rest of this work, we only show the results for the case where the two galaxies are allowed to move freely.

The best-fit stream tracks for the three halo shapes obtained in the presence of the LMC as well as one stream model with the LMC excluded are shown in Figure 3. As is obvious from the Figure, the addition of the LMC allows us to adequately match the overall properties of the OS across the entire sky. Some minor discrepancies still exist, mainly in the behavior of the stream on the sky (top panel). It is also clear that a spherical Milky Way provides a poor match to the OS data, especially the oscillation in the stream track around $\phi_1 \sim 100^\circ$. Allowing the halo to be axisymmetric (either prolate or oblate) brings the model into a better agreement with the data. For reference we also show the best-fit OS model in the Milky Way without the LMC (dotted orange line). This fit was carried out using a setup identical to that described in Section 3 except

that we place the progenitor at $\phi_1 = 6.34^\circ$ and fit the entire data range. While the Milky Way-only model does a reasonable job for some of the observables for a range of ϕ_1 , it fails miserably in predicting the positions of the OS debris on the sky.

In Figure 4, we present the stream particles in the best-fit stream model in a prolate, reflexive Milky Way potential. The left panel shows the stream observables, which are all a close match to the sample of RR Lyrae stars from *Gaia* DR2. The top right panel compares the ratio of the reflex corrected proper motions and the stream track, mimicking the presentation in Figure 1. We see that the best-fit model has the same misalignment as the observed stream. The bottom right panel gives the closest approach distance to the LMC for each particle in the stream (note the logarithmic scale of the y-axis). We see that the trend is nearly monotonic with stream particles with smaller ϕ_1 experiencing a closer approach and therefore a stronger interaction with the LMC than those with larger ϕ_1 . This explains why the largest misalignments are seen for $\phi_1 < 0^\circ$ since this is where the effect of the LMC is the strongest. These closest approaches are not simultaneous but happen over a range of times from 350 Myr ago ($\phi_1 \sim -90^\circ$) to 100 Myr ago ($\phi_1 \sim 0^\circ$). Thus, we see that the perturbation from the

Parameter	sph. MW+LMC	obl. MW+LMC	pro. MW+LMC	sph. rMW+LMC	obl. rMW+LMC	pro. rMW+LMC
$M_{\text{NFW}} (10^{11} M_{\odot})$	$13.1^{+5.0}_{-3.9}$	$13.2^{+3.0}_{-2.3}$	$12.7^{+3.0}_{-2.4}$	$7.7^{+1.0}_{-1.1}$	$11.3^{+2.2}_{-2.3}$	$9.4^{+1.5}_{-1.0}$
r_s (kpc)	$24.1^{+7.1}_{-6.0}$	$22.3^{+4.0}_{-3.1}$	$21.8^{+3.5}_{-2.9}$	$12.7^{+2.1}_{-2.2}$	$21.9^{+3.1}_{-3.8}$	$17.5^{+2.2}_{-1.8}$
q_{NFW}	—	$0.89^{+0.02}_{-0.03}$	$1.19^{+0.03}_{-0.03}$	—	$0.87^{+0.04}_{-0.04}$	$1.20^{+0.04}_{-0.03}$
$l_{\text{NFW}} (^{\circ})$	—	$17.5^{+8.4}_{-11.9}$	$94.2^{+6.9}_{-7.5}$	—	$-3.8^{+17.3}_{-34.2}$	$95.5^{+6.3}_{-8.6}$
$b_{\text{NFW}} (^{\circ})$	—	$-4.0^{+15.8}_{-13.6}$	$37.2^{+8.1}_{-6.8}$	—	$13.1^{+13.9}_{-15.1}$	$32.0^{+5.4}_{-4.5}$
$M_{\text{LMC}} (10^{11} M_{\odot})$	$1.26^{+0.25}_{-0.24}$	$1.13^{+0.22}_{-0.20}$	$1.02^{+0.16}_{-0.13}$	$1.49^{+0.28}_{-0.24}$	$1.41^{+0.35}_{-0.33}$	$1.38^{+0.27}_{-0.24}$
$\Delta \log \mathcal{L}$	-81	-43	-13	-47	-25	0
$M_{\text{MW}}(50 \text{ kpc}) (10^{11} M_{\odot})$	$4.18^{+0.22}_{-0.23}$	$4.18^{+0.19}_{-0.25}$	$4.13^{+0.23}_{-0.25}$	$4.04^{+0.10}_{-0.10}$	$3.74^{+0.19}_{-0.22}$	$3.80^{+0.14}_{-0.11}$

Table 2. Posteriors on our Milky Way and LMC properties. We give the posteriors for 6 different setups which include the LMC. For each parameter, we give the median with 1σ uncertainties. For reference, the $\Delta \log \mathcal{L}$ for our best fit without the LMC shown in Fig. 3 is -457. We do not give any parameters for fits without the LMC since these fits are so poor that the result is not meaningful. The first 3 columns show the results of fits with a spherical, oblate, and prolate halo with a fixed Milky Way which cannot respond to the LMC. The next 3 columns show fits with reflexive models where the Milky Way can move in response to the LMC. These models are denoted as rMW. The best likelihood for the reflexive, prolate halo. Interestingly, the fits with reflexive haloes require a higher LMC mass of $\sim 1.4 \times 10^{11} M_{\odot}$. For reference, the LMC’s orbital plane corresponds to $(l_{\text{NFW}}, b_{\text{NFW}}) = (-4.5^{\circ}, 5.4^{\circ})$, the orientation of the best-fit halo in Law & Majewski (2010) corresponds to $(l_{\text{NFW}}, b_{\text{NFW}}) = (7^{\circ}, 0^{\circ})$, and the current orientation of the LMC corresponds to $(l_{\text{NFW}}, b_{\text{NFW}}) = (89.1^{\circ}, 33.3^{\circ})$. Curiously, these directions are close to the best-fit halo orientations. The maximum-likelihood values for each of these setups are given in Tab. A1.

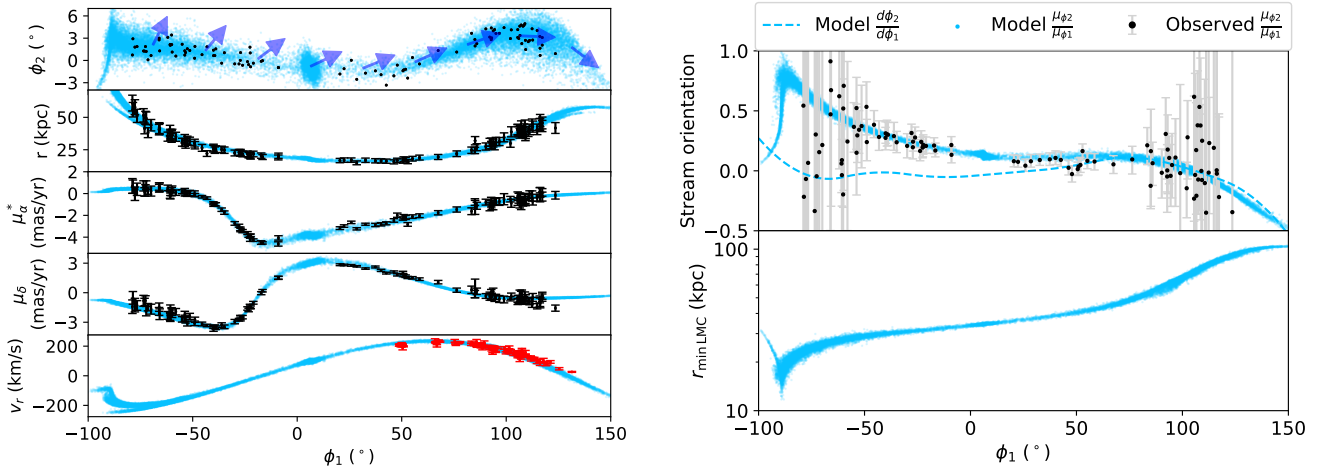


Figure 4. Best-fit stream in a prolate Milky Way halo. **Left panel:** From top to bottom, the panels show the stream on the sky (in coordinates aligned with the stream), heliocentric distance to the stream, proper motion in RA, proper motion in Dec, and radial velocity of the stream. The black points show the RR Lyrae from *Gaia* DR2. The red points with error bars in the bottom panel show the radial velocity of stars in the stream. Note that these radial velocities were not used in the fits. **Right panel:** In the top panel, the blue points show the ratio of reflex corrected proper motions in the best-fit stream, the black points with error bars show the same ratio for the RR Lyrae, and the dashed-blue line show the slope of the best-fit stream track. The model clearly reproduces the misaligned proper motions seen in the observed stream (see Fig. 1). The bottom panel shows the closest approach distance to the LMC versus angle along the stream. The left-most portion of the stream has a much more intimate interaction with the LMC which explains why the proper motion offset is largest there. Thus, the misalignment in the OS can be naturally explained by including the LMC.

LMC can naturally explain the misalignment seen in the OS. This best-fit stream and its orbit are publicly available [here](#).

Figure 5 shows the residuals of the best-fit model from Figure 4. For each RR Lyrae and each observable, we plot the model value minus the observed value. Overall, there are almost no significant residuals showing that the best-fit model is a good representation of the data. However, there is a small residual in $\Delta\mu_{\delta}$ between $50^{\circ} < \phi_1 < 75^{\circ}$. Interestingly, this lines up with an underdensity seen in RR Lyrae (see Fig. 15 in Koposov et al. 2019).

As an alternative way to visualize the effect of the LMC, we show the 3D projections of the OS data (black filled circles), our best-fit OS model (blue points), the corresponding progenitor’s orbit (dashed blue line) and the LMC’s orbit (dotted green line) in Figure 6. The present day position of the LMC is marked with

large filled green circle. The three panels show the projections in Galactocentric Cartesian coordinates. As the Figure demonstrates, the model stream lines up with the progenitor’s orbit in the Galactic North. However, in the South, the OS appears to be pulled away from its orbit towards the orbit of the LMC. Of course, these projections only show the present day location of the stream. A movie showing the disruption of the OS in a static, spherical Milky Way halo in the presence of the LMC can be found at <https://youtu.be/sBKpwQR7JJQ>.

Figure 7 show the posterior distributions of the Milky Way and LMC parameters for our best-fit halo, namely a reflexive, prolate Milky Way halo. The distributions of individual parameter values look single-peaked and well-behaved. There is also a familiar degeneracy between the scale-radius and the DM halo mass of the

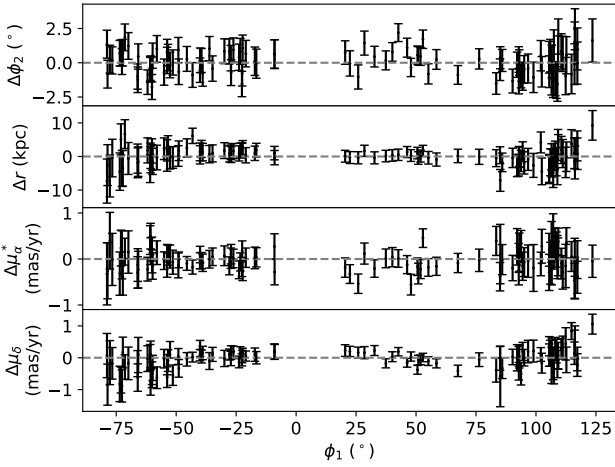


Figure 5. Residuals of best fit model shown in Fig. 4. In each panel we plot the model value minus the observed value and highlight the value of zero with a dashed-grey line. The error bars come from summing the model width and observed errors in quadrature. There are no significant residuals apart from an offset in $\Delta\mu_\delta$ between $50^\circ < \phi_1 < 75^\circ$.

Milky Way. This is likely because the OS is in the outskirts of the Milky Way and thus it is not sensitive to the inner profile of the halo. The fits favor a Milky Way mass of $9.4 \times 10^{11} M_\odot$ although the posteriors are quite broad at the 2σ level. Most interestingly, we get a tight constraint on the LMC mass of $1.38^{+0.24}_{-0.27} \times 10^{11} M_\odot$. Thus, for the first time we have a robust measurement of the LMC mass from its effect on a Milky Way stream.

The posteriors of all of our fits are given in Table 2. Curiously, in the case of flattened haloes, the fits prefer a significantly aspherical halo: in the prolate case, a flattening of $q_{\text{NEW}} \sim 1.20$ is inferred, while in the oblate case, the model converges to $q_{\text{NEW}} \sim 0.87$. In addition, the fits also prefer a particular orientation. In the prolate case, the halo is stretched towards roughly the present-day location of the LMC. In the oblate case, the flattened axis of the halo is within $\sim 20^\circ$ of the orbital plane of the LMC. Interestingly, the orientation in the oblate case is consistent with the results Law & Majewski (2010) who fit the Sagittarius stream and found an almost axisymmetric, oblate halo flattened close to the LMC’s orbital plane. We will discuss the significance of these results more in Section 5. The maximum-likelihood values for each of these setups are given in Table A1.

4.3 Orbit of Orphan and the LMC

We find that the orbit of the Orphan stream progenitor changes significantly before and after the LMC’s infall, and that it depends on how we treat the Milky Way halo. For example, in the case of a fixed, prolate halo, the orbit has a pericenter of ~ 23 kpc and an apocenter of ~ 79 kpc before the LMC’s infall. Just after infall, this pericenter is reduced to ~ 16 kpc. In a prolate halo with a reflexive Milky Way, the pericenter and apocenter before the LMC’s infall are ~ 23 kpc and ~ 71 kpc respectively while the post-infall pericenter is ~ 16 kpc. In contrast, for a spherical, reflexive halo, the pre-infall pericenter and apocenter are ~ 28 kpc and ~ 59 kpc respectively, while the post-infall pericenter is again ~ 16 kpc. Thus we see that the Orphan progenitor was on a less eccentric orbit before interacting with the LMC. However, we note that since the

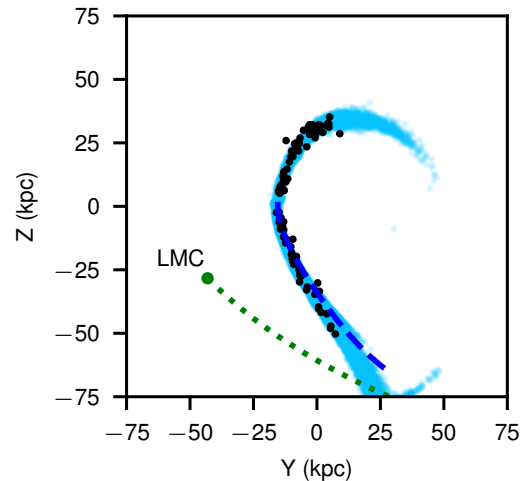
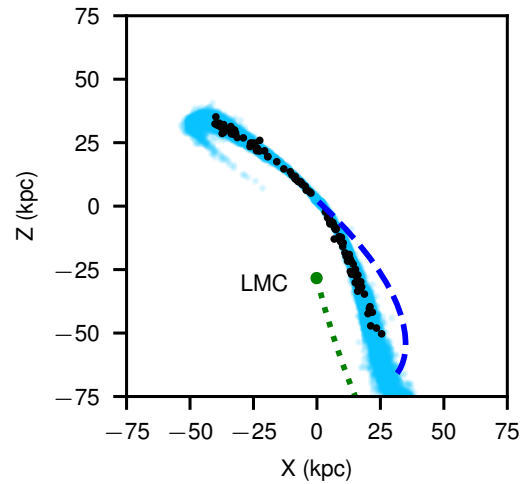
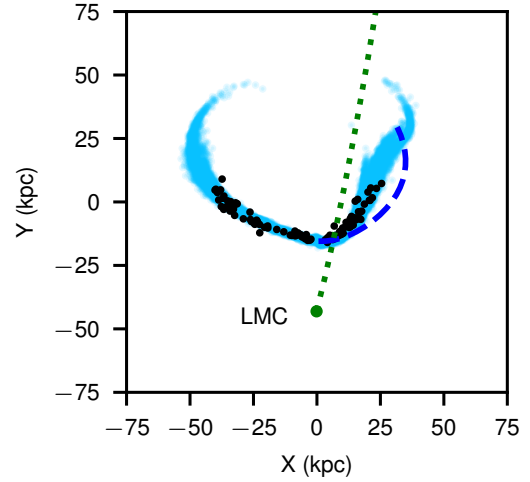


Figure 6. Best fit model from Fig. 4 shown in 3d in Galactocentric coordinates. From top to bottom, the panels show the XY, XZ, and YZ projections. In each panel, the light blue points show the model stream, the black points show the RR Lyrae positions, the dashed-blue lines show the orbit of the progenitor, and the dotted green line shows the orbit of the LMC. The LMC’s nearby passage pulls the stream away from its orbit which leads to the offset seen in Fig. 1.

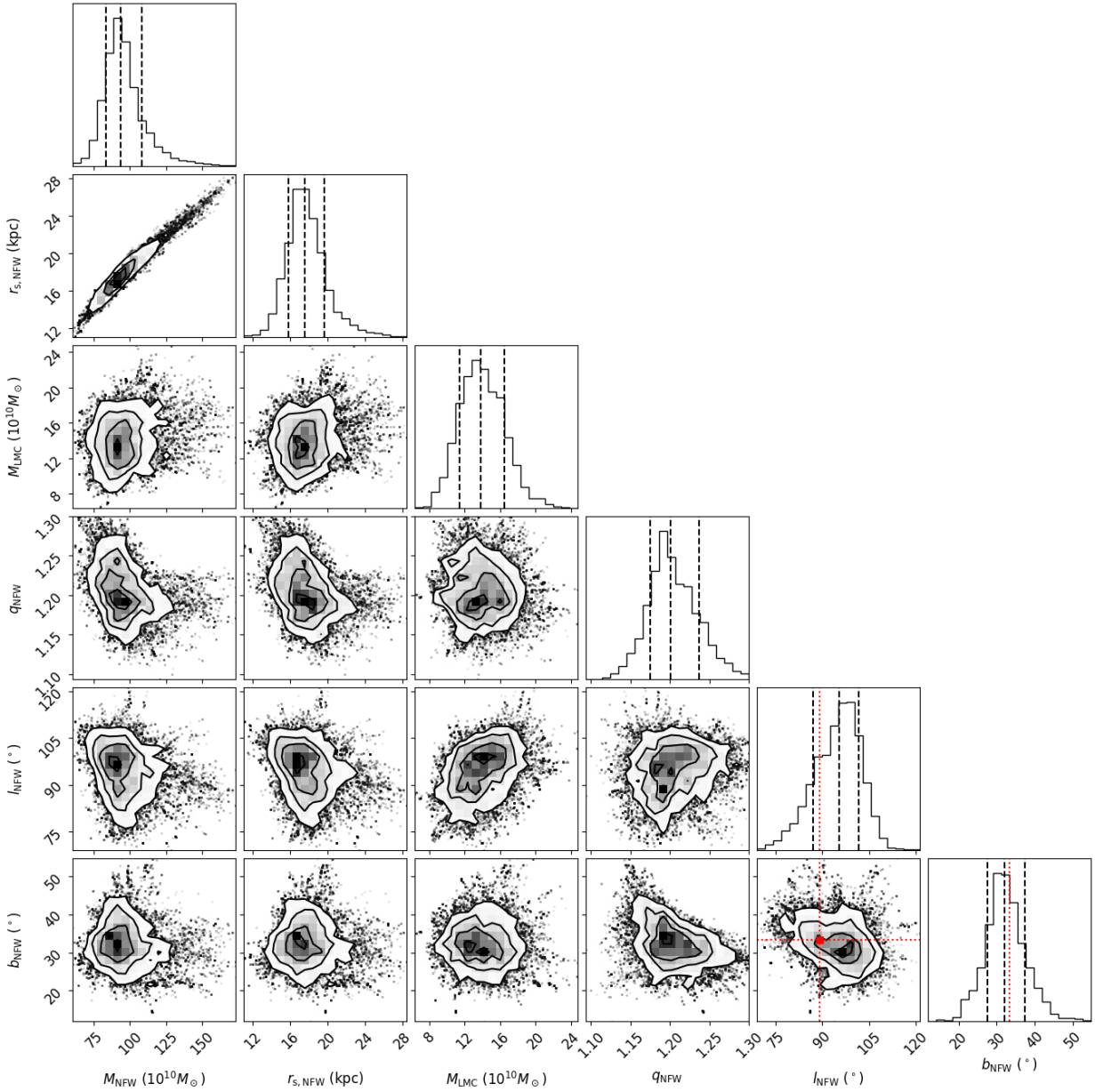


Figure 7. Posteriors in fixed, prolate Milky Way potential with LMC. In each of the diagonal posteriors, we show the median with the $\pm 1\sigma$ range. The red point in the bottom right figure shows the direction corresponding to the LMC’s present day location from the galactic center. Interestingly, the flattening is closely aligned with the direction towards the LMC suggesting that it may be related to the LMC.

effect of the LMC varies strongly along the stream (see Fig. 4), the change in the orbit of each star will likewise vary along the stream. For example, stars in the South which have been most affected by the LMC have been pulled out beyond 95 kpc while stars in the North have been affected much less.

We have also checked whether the LMC has additional pericentric passages over the past 5 Gyr. In the prolate, reflexive halo, the median time at which the LMC reaches its apocenter is 3.6 Gyr ago but none of the chains have an LMC which has an additional pericenter in the past. In the spherical, reflexive halo, the median apocenter is 3.6 Gyr with 1.6% of our chains having an additional pericenter close to 5 Gyr ago. Thus, in the vast majority of cases, the LMC only has a strong effect on Orphan in the recent past. In

the few cases that the LMC does have an additional interaction, this will have little effect on the present day properties of Orphan in our model since only a small fraction of the stars in Orphan would have stripped by those early times. In addition, since the stream grows in time, these stars would be far from the progenitor and thus outside the observed region.

4.4 Mass constraint on the Milky Way

Finally, we compare our constraint on the Milky Way mass profile with existing results in Figure 8. Despite the broad posteriors in Figure 7, the constraint on the Milky Way mass as a function of radius is remarkably tight. Our results also agree with existing results

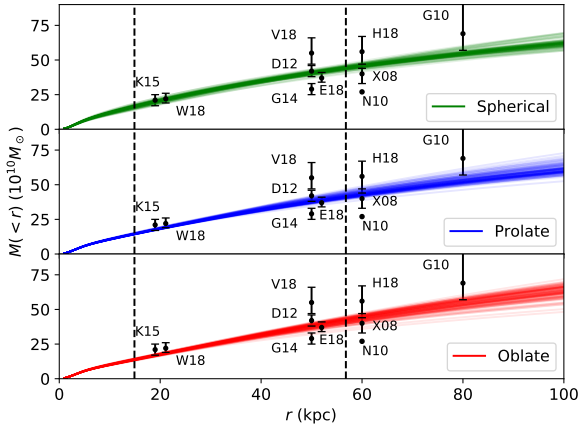


Figure 8. Mass constraint for total Milky Way mass as a function of radius. From top to bottom, we show samples from our MCMC chains in a spherical, prolate, and oblate halo which can respond to the LMC. In each panel, the black points with error bars show measurements from Deason et al. (2012) (D12), Eadie & Jurić (2018) (E18) Gnedin et al. (2010) (G10), Gibbons, Belokurov & Evans (2014) (G14), Hendel et al. (2018) (H18), Küpper et al. (2015) (K15), Newberg et al. (2010) (N10), Vasiliev (2019) (V18), Watkins et al. (2018) (W18), and Xue et al. (2008) (X08). Note that N10 did not provide an error bar on their result and we have shifted E18 from 50 kpc for clarity. The dashed-black vertical lines show the radial extent of the Orphan RR Lyrae sample from Kopusov et al. (2019) fit in this work.

in the literature, although with a tendency to prefer lower values of the total mass. Note that when computing the mass enclosed in Figure 8, we have ignored the flattening of the halo. For reference, we also give the mass enclosed within 50 kpc in Table 2. As expected from Figure 8, this mass is remarkably well constrained. This is due to the wealth of RR Lyrae uncovered by Kopusov et al. (2019) and the precise multi-dimensional data from *Gaia* DR2.

5 DISCUSSION

5.1 Limitations of this analysis

In this work we have shown that the observed phase-space properties of the OS can be well-modelled if we include the effect of the LMC. We have attempted to fit Orphan without the LMC and the result is rather spectacularly poor (see Fig. 3) due to the misalignment of the stream with its proper motions. While we only considered one form for the potential, we argue that in general, this offset cannot be reproduced in a static potential. In this context, we note that (Sanders & Binney 2013) studied streams in action-angle space and showed that there is a misalignment between streams and orbits in action-angle space. However, they found that in their chosen Milky Way potential, the OS should have the smallest misalignment. We can also compare the size of the velocity component perpendicular to the stream (~ 60 km/s from Kopusov et al. 2019) to the expected velocity dispersion of the progenitor at its tidal radius. Assuming a progenitor mass of $10^7 M_\odot$ and a pericenter of 15 kpc, this would correspond to a tidal radius of 493 pc and thus a velocity dispersion of ~ 5 km/s in *MWPotential2014* from Bovy (2015). Since this is significantly smaller than the measured velocity offset, we do not think it is possible to produce such an offset in any static potential. Note that our assumed progenitor mass is based on the total stellar mass in the OS estimated in Kopusov et al. (2019). Although the

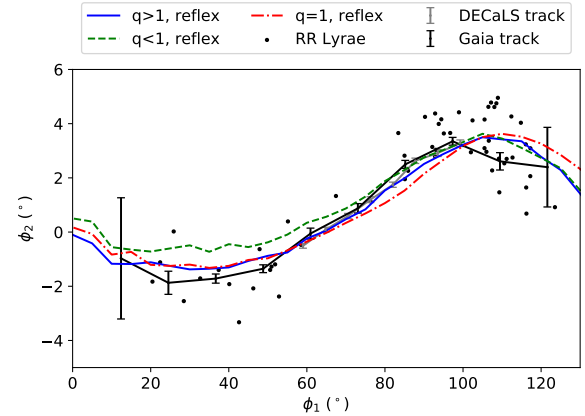


Figure 9. Comparison of RR Lyrae and stream track from Kopusov et al. (2019) with our best-fit models.

OS progenitor was much more massive than this originally, by the time the stellar stream formed, almost all of the dark matter would have already been stripped.

In the analysis in Sections 3, 4 we have fit the RR Lyrae sample from Kopusov et al. (2019). However, Kopusov et al. (2019) also measured the track using Red Giant Branch (RGB) stars from *Gaia* DR2 and RGB/Main Sequence Turn-Off stars in DECaLS. We show these tracks with our best-fit streams in Figure 9. Interestingly, we see that in the regions where the tracks and RR Lyrae positions appear to slightly disagree ($\phi_1 \sim 100^\circ$), our best-fit models appear to follow the tracks in these other tracers. Since both the prolate and oblate haloes are a better fit to the RR Lyrae in this range, this could suggest that fits to the stream tracks (instead of the individual RR Lyrae positions) might prefer a more spherical halo.

5.2 Interpretation of the LMC mass

In this work we have shown that including an LMC with a substantial mass is essential for understanding the behavior of the OS. The models used in this work have all treated the LMC mass as being fixed in time. In reality, as the LMC falls onto the Milky Way, the dark matter in its outskirts will be tidally stripped, changing the mass profile and shape of the LMC. Note that this stripped material will still exert a force on the Milky Way and the OS so accounting for the stripping is not as simple as just removing the mass. Accordingly, we surmise that this work constrains an effective mass for the LMC which captures its effect on the OS. Since the LMC is believed to be on its first approach (e.g. Besla et al. 2007; Kalliyayalil et al. 2013), this mass should not be too different from the peak mass of the LMC although future work is needed to better understand their relation.

5.3 Interpretation of Milky Way halo shape

The best-fit models to the OS in Section 4 require that the Milky Way halo must be substantially aspherical. We considered axisymmetric haloes with a flattening in an arbitrary direction. For prolate haloes, we found a halo with an elongation that is roughly aligned with the present day position of the LMC. For oblate haloes, we found a halo with a flattening roughly aligned with the orbital plane of the LMC. The oblate halo shape is especially interesting given

its similarity with [Law & Majewski \(2010\)](#) who studied the Sagittarius stream and found a very similar orientation. Thus, the only two streams that probe the outskirts of the Milky Way both point to a similarly flattened halo in the outskirts. If this is the case, it would have important implications for the plane of satellites since this plane can be long-lived if it is aligned with the short or long axis of the halo ([Bowden, Evans & Belokurov 2013](#)). We note that although [Law & Majewski \(2010\)](#) considered triaxial haloes, they forced the halo to have one flattening in the Galactic z direction so we cannot directly compare their result with our prolate halo.

In order to better understand the effect of the LMC on the Milky Way halo, we show projections of an N -body simulation of the LMC accreting onto the Milky Way in [Figure 10](#). These simulations are taken from [Laporte et al. \(2018\)](#) who simulate a $2.5 \times 10^{11} M_{\odot}$ LMC on its first infall onto the Milky Way. The LMC in this model ends up within 2σ of its observed phase-space position. The top (bottom) panels show the XY (YZ) projection of a 20 kpc slab centered on $Z=0$ ($X=0$) from the snapshot which matches the LMC at the present day. Interestingly, the Milky Way appears to be mostly spherical (left panels) while the LMC has been significantly tidally disrupted by the Milky Way (middle panel). The orbit of the LMC and the RR Lyrae from [Koposov et al. \(2019\)](#) are also shown for reference.

While we have shown that the OS requires a substantially aspherical halo shape for the Milky Way, we must be careful in interpreting the meaning of this. One possibility is that this reflects the long term shape of the Milky Way halo. Indeed, simulations of Milky Way-like galaxies have shown that haloes can have axis ratios of 0.6-0.8 in density even when baryonic processes are included (e.g. [Zhu et al. 2016](#)). Such a flattening is consistent with our oblate haloes which have a flattening of $q \sim 0.9$ in the potential. However, in this case, the Milky Way disk would need to be aligned with the short or long axis of the halo to be stable ([DeBattista et al. 2013](#)). This would be an issue for our prolate halo solution which is substantially misaligned with the disk. However, since Orphan is only probing the halo beyond ~ 10 kpc, the halo could have a different shape in the inner regions and the shape we find here in the outskirts. Thus, the disk could still be made stable in this scenario.

A second possibility is that the shape we find here reflects the response of Milky Way's halo to the infall of the LMC ([Weinberg 1989](#)). This effect was investigated in [Vesperini & Weinberg \(2000\)](#) who showed that the infall of satellites can induce substantial density features in the host halo. Similarly, [Gómez et al. \(2016\)](#) investigated accretion events in cosmological zoom-in simulations and found that the density of the host halo can be substantially perturbed which would lead to torques on structures within the host halo larger than those expected from the perturber itself. Despite the high relative velocity of the LMC, the same mechanism is still able to operate on the the Milky Way, notably warping the disk ([Laporte et al. 2018](#)). This interpretation is further supported by the fact that the halo shapes we infer are aligned with either the present day position of the LMC (prolate halo) or with the orbital plane of the LMC (oblate halo). However, as we can see from [Figure 10](#), this is not expected to generate an extremely flattened Milky Way.

Finally, it is possible that the halo shape we infer is not due to the Milky Way but is rather capturing an effect from the LMC which is not correctly modelled by treating the LMC as a non-deforming Hernquist sphere. As with the previous explanation, this is supported by the fact that the halo shapes are related to either the LMC's present day position or orbital plane. One effect we are neglecting is the tidal disruption of the LMC by the Milky Way which

will dramatically stretch the dark matter distribution in the outskirts of the LMC (e.g. middle panels of [Fig. 10](#)). We are also ignoring the SMC which could have an additional affect on Orphan. However, as we argued above, since the SMC has already been substantially disrupted by the LMC, its present-day mass should be quite small.

5.4 The impact of the LMC on other structures in the Milky Way

For the first time, we have measured the significant impact of the LMC on a structure in the Milky Way. The LMC has three main effects on structures orbiting our Galaxy. First, structures which pass near the LMC will feel a large force which will directly change their dynamics. Second, the LMC will induce a reflex motion in the Milky Way itself ([Gómez et al. 2015](#)) which can affect structures in our Galaxy. Third, the LMC can deform the Milky Way halo, resulting in additional tidal forces (e.g. [Weinberg 1998](#); [Weinberg & Blitz 2006](#)).

These effects have wide ranging implications for any technique which attempts to precisely measure the properties of the Milky Way by studying tracers orbiting our Galaxy, e.g. equilibrium modeling of GCs (e.g. [Watkins, Evans & An 2010](#); [Vasiliev 2019](#)), the stellar halo ([Xue et al. 2008](#); [Deason et al. 2012](#)), or hypervelocity stars ([Gnedin et al. 2005](#)). All of these techniques should be revisited in light of the increased LMC mass to understand how the results may be biased by ignoring the presence of our largest - and most massive - satellite.

Along these lines, [Laporte et al. \(2018\)](#) have studied the effect of the LMC on its first infall ([Besla et al. 2007](#)) on the Milky Way's disk using live high-resolution N -body simulations. They found that the response of the halo can result in strong overdensities of up to 50% within ~ 40 kpc penetrating into the inner regions of the Galaxy, resulting in torques warping the disk with similar shape and line of nodes as the observed HI warp ([Levine, Blitz & Heiles 2006](#)), in agreement with earlier expectations from linear perturbation theory (e.g. [Weinberg 1998](#); [Weinberg & Blitz 2006](#)). The impact of the Milky Way's dark matter halo response to the LMC on tracer kinematics in the halo are explored further in [Garavito-Camargo et al. \(2019\)](#).

Given the large effect seen in this work, we expect that many other streams will exhibit similar effects from the LMC. The streams in the Southern Galactic hemisphere are natural candidates since they have had closer passages with the LMC. Tucana III is an especially good candidate given its close passage with the LMC ([Erkal et al. 2018](#); [Simon 2018](#); [Fritz et al. 2018](#)), as are the 11 streams recently discovered in the Dark Energy Survey ([Shipp et al. 2018](#)). Since these streams will each have a different closest approach to the LMC, they can be used to measure the LMC's radial density profile and shape. Such modelling would not be simple as it would need to account for the time-dependent LMC shape due to its disruption by the Milky Way.

The substantial LMC mass found in this work suggests that the LMC has brought a large number of satellite galaxies into the Milky Way ([Sales et al. 2011](#)). Indeed, the LMC group infall was proposed by [Jethwa, Erkal & Belokurov \(2016\)](#) to explain the abundance of satellites found in the Dark Energy Survey. Recently, [Kallivayalil et al. \(2018\)](#) confirmed this prediction and found 4 ultra-faint dwarfs which were likely accreted with the LMC, in addition to the SMC which was previously argued to have fallen in with the LMC (e.g. [Kallivayalil et al. 2013](#)). Given that [Jethwa, Erkal & Belokurov \(2016\)](#) predicted the LMC could have brought up to ~ 70 satellites, we expect that many more satellites will be found in the

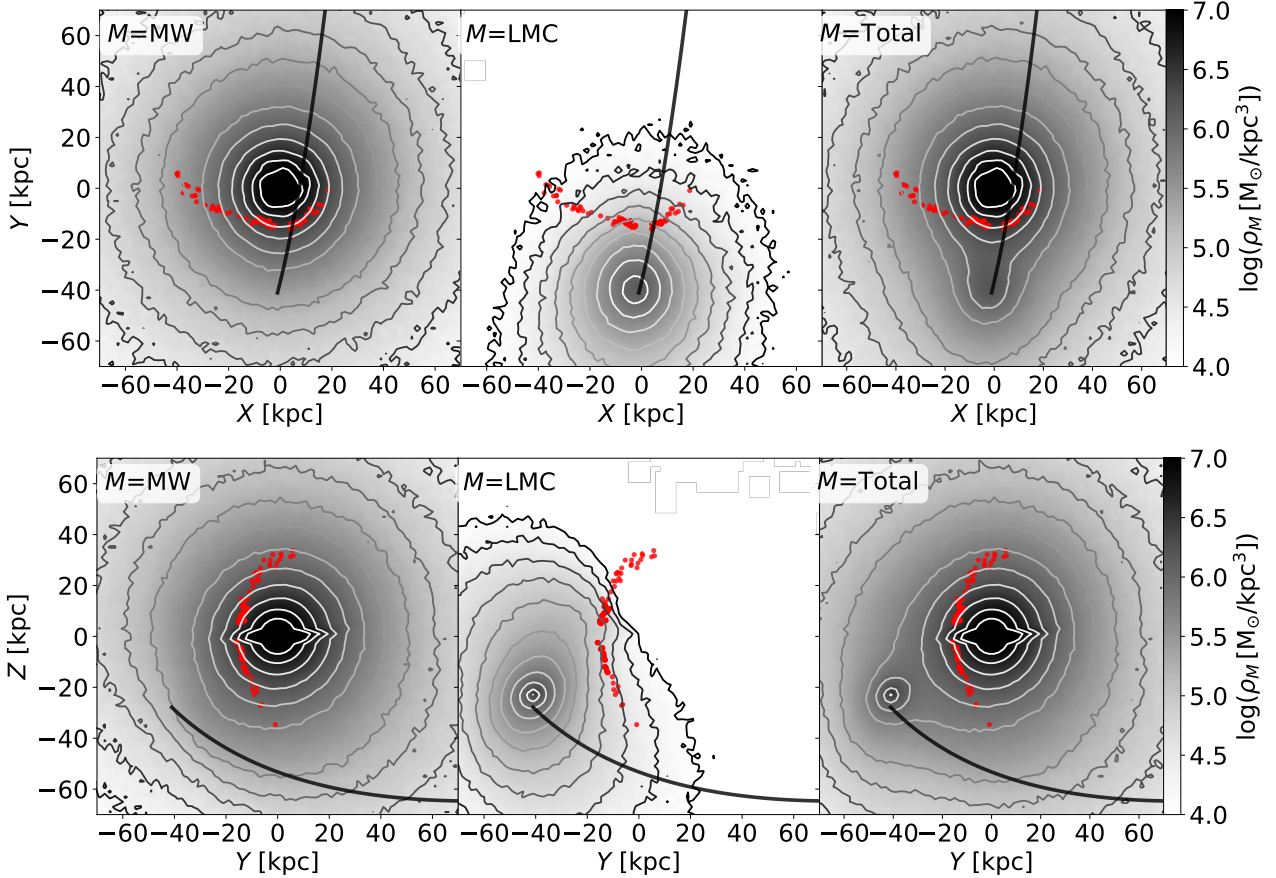


Figure 10. Density of Milky Way and LMC in N -body simulation from Laporte et al. (2018). The top three panels show an XY projection of a 20 kpc thick slab centered on $Z = 0$ in Galactocentric coordinates. The bottom three panels show YZ projections show a 20 kpc thick slab centered on $X = 0$. The left, middle, and right panels show projections of the Milky Way, LMC, and the combined Milky Way-LMC densities respectively. The orbit of the LMC is shown as a black line and the RR Lyrae from Koposov et al. (2019) are shown as red points. Although the LMC is heavily distorted by the Milky Way (middle panels), the Milky Way itself remains remarkably spherical on average (left panels). This is in contrast to our best-fit prolate and oblate models which have significant flattenings of $q = 1.20$ and $q = 0.87$ in the potential, respectively (see Tab. 2).

coming years. The phase-space positions of this large number of satellites will provide another avenue for measuring the LMC mass.

Finally, we can use the results of this work in order to assess the importance of the reflex motion of the Milky Way. In Figure 11 we compare the expected reflex motion over the past 2 Gyr with the orbital timescales in the Milky Way. The blue lines show the reflex motion of the Milky Way in 100 samples of the MCMC chains used to fit Orphan in a prolate Milky Way halo. These should be compared with the dashed-black curve which shows the orbital period versus radius for circular orbits in the Milky Way in *MWPotential2014* from Bovy (2015). Stars for which the orbital timescale is much smaller than the timescale over which the Milky Way moves by a distance equal to the orbital radius (i.e. those to the left of the blue curves) will respond adiabatically to the LMC’s passage and will move with the reflex velocity of the Milky Way. However, stars on orbits for which the orbital timescale is longer than the timescale over which the Milky Way moves by their orbital radius (i.e. those to the right of the blue curves) will continue on their original orbits and should consequently have a velocity relative to the Milky Way itself. We thus expect that there is a region within the Milky Way ($r < \sim 30$ kpc) which will respond adiabatically during the LMC’s infall. However, beyond this radius, the stars will not have had time to adjust to the Milky Way’s velocity

after the LMC’s infall and should have a velocity (~ 40 km/s) relative to interior part of the Milky Way. Since the majority of the Milky Way’s reflex motion is downwards, we predict that the outer regions of the Milky Way should have an upwards velocity relative to the inner regions. This effect should be visible in the outskirts of the Galactic stellar halo.

6 CONCLUSIONS

Motivated by the new observational constraints recently presented by Koposov et al. (2019), this Paper presents the results of a comprehensive modelling of the Orphan stream. Our analysis relies on the rapid and accurate model stream production implemented using the mLCS technique (Gibbons, Belokurov & Evans 2014) and considers a wide range of Galactic Dark Matter halo configurations. Taking advantage of the efficiency and the flexibility of our stream models, we are also able to include the presence of the Large Magellanic Cloud as well as the reflex motion of the Milky Way in response to the dwarf’s infall. For the first time, we have unveiled an unambiguous perturbation exerted by the Large Magellanic Cloud on a stellar stream within the Milky Way. In our reconstruction of the encounter, as the LMC was falling into the Galaxy, it passed

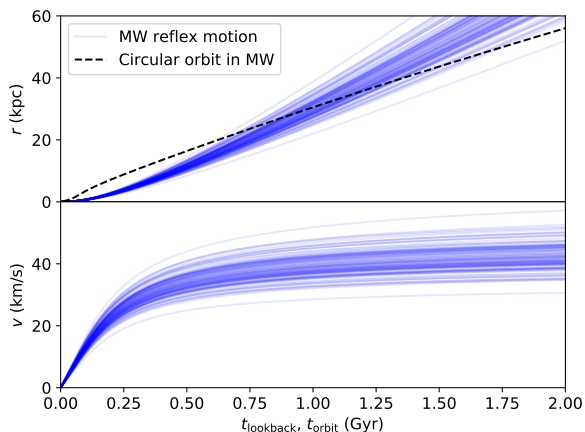


Figure 11. Reflex motion of the Milky Way compared to orbital timescales in the Milky Way. The blue lines show the reflex motion of the Milky Way from 100 samples of the chains in the prolate halo fits. In the top (bottom) panel, these blue lines show the distance (speed) of the Milky Way moves relative to its present day position (velocity). The dashed-black line shows the orbital period versus radius for circular orbits in the Milky Way. Stars on orbits to the left of the blue lines can respond adiabatically to the LMC’s infall and thus should move with the Milky Way’s reflex velocity. However, stars on orbits to the right of the blue curves will not have time to respond to the Milky Way’s motion and will remain on their original orbits.

near the Orphan stream and pulled the stream off its original path. The resulting deflection is so large that it can be seen in the data itself as a misalignment of the Orphan stream track and the direction of its proper motions (see Fig. 1). Detecting this effect was only possible with the exquisite data quality in *Gaia* DR2 which offers an all-sky view of the RR Lyrae across the entire Milky Way, including their proper motions.

Without the presence of the LMC, it is only possible to reproduce the phase-space track of the stream in the North, i.e. for $\phi_1 > 50^\circ$. The Southern Galactic portion of such a model is an extremely poor fit to the data (see Fig. 2). However, taking the same model and including an LMC with a modest mass results in a significant deflection of the Southern portion of the stream. Furthermore, if the LMC mass is increased to $\sim 10^{11} M_\odot$, this deflection grows and the resulting stream is a good match to the Orphan data over the entire range of along-stream coordinate ϕ_1 . Interestingly, this exercise shows that while the LMC’s main effect is on the Southern portion of Orphan, there is also a noticeable deflection of the Northern OS debris suggesting that the LMC’s influence will be felt across the Galaxy.

In order to measure the LMC mass, we fit the entire range of the Orphan stream including the LMC mass as a parameter in our fits. These fits are performed with an axisymmetric Milky Way halo which can be flattened in any direction. The fits require LMC masses between $1 - 1.5 \times 10^{11} M_\odot$ depending both on whether we have a spherical, oblate, or prolate halo and on whether we allow the Milky Way halo to respond to the LMC’s infall. Curiously, the fits in an oblate and prolate halo prefer halo shapes which appear to be aligned with either the LMC’s orbital plane or the LMC’s present day location respectively. In these cases, we suspect that the Milky Way halo may be compensating for some aspect of the LMC’s effect which we have not correctly modelled, e.g. the tidal disruption of the LMC by the Milky Way. This may suggest that the LMC is more massive than our results imply, although we note that fits in a spherical halo can also match the Orphan stream.

The implications of our measurement of the LMC mass are far reaching. Any technique which has assumed that the Milky Way is in equilibrium should be revisited to determine how the LMC will bias its results. As one concrete example of such an effect, we predict that the outskirts of the Milky Way ($r > \sim 30$ kpc) will have a bulk upwards velocity (~ 40 km/s) relative to the Sun due to the reflex response of our Galaxy. If the results of this work are correct, future efforts with *Gaia* DR2 should reveal a significantly perturbed Milky Way.

We note that in the final stages of preparing this manuscript, [Fardal et al. \(2018\)](#) released their analysis of the Orphan stream. Their work focused on the Northern portion of the Orphan stream and showed that there was a misalignment between the stream track and its velocity vector.

ACKNOWLEDGEMENTS

We thank the streams group at Cambridge and Eugene Vasiliev for helpful comments which improved the clarity of this work. DE thanks Michelle Collins and Shu Kim for insightful discussions. We thank the anonymous referee for their thoughtful comments which have improved the clarity of this work. This work was started at the Aspen Center for Physics, which is supported by National Science Foundation grant PHY-1607611. We thank Michael for an illuminating discussion. The research leading to these results has received funding from the European Research Council under the European Union’s Seventh Framework Programme (FP/2007-2013) / ERC Grant Agreement n. 308024. SK is partially supported by NSF grant AST-1813881. NK is supported by NSF CAREER award 1455260.

This work presents results from the European Space Agency (ESA) space mission *Gaia*. *Gaia* data are being processed by the *Gaia* Data Processing and Analysis Consortium (DPAC). Funding for the DPAC is provided by national institutions, in particular the institutions participating in the *Gaia* MultiLateral Agreement (MLA). The *Gaia* mission website is <https://www.cosmos.esa.int/gaia>. The *Gaia* archive website is <https://archives.esac.esa.int/gaia>.

This research made use of IPYTHON ([Perez & Granger 2007](#)), python packages NUMPY ([van der Walt, Colbert & Varoquaux 2011](#)), MATPLOTLIB ([Hunter 2007](#)), and SCIPY ([Jones et al. 2001–](#)). This research also made use of Astropy,¹ a community-developed core Python package for Astronomy ([Astropy Collaboration et al. 2013; Price-Whelan et al. 2018](#)).

REFERENCES

- Aaronson M., 1983, *ApJ*, 266, L11
- Agnello A., Evans N. W., 2012, *ApJ*, 754, L39
- Amorisco N. C., Martinez-Delgado D., Schedler J., 2015, arXiv e-prints, arXiv:1504.03697
- Astropy Collaboration et al., 2013, *A&A*, 558, A33
- Auger M. W., Treu T., Bolton A. S., Gavazzi R., Koopmans L. V. E., Marshall P. J., Moustakas L. A., Burles S., 2010, *ApJ*, 724, 511
- Behroozi P. S., Wechsler R. H., Conroy C., 2013, *ApJ*, 770, 57
- Belokurov V., Erkal D., Deason A. J., Koposov S. E., De Angeli F., Evans D. W., Fraternali F., Mackey D., 2017, *MNRAS*, 466, 4711
- Belokurov V. et al., 2007, *ApJ*, 658, 337
- Belokurov V., Koposov S. E., 2016, *MNRAS*, 456, 602

¹ <http://www.astropy.org>

- Belokurov V. A., Erkal D., 2019, *MNRAS*, 482, L9
- Besla G., Kallivayalil N., Hernquist L., Robertson B., Cox T. J., van der Marel R. P., Alcock C., 2007, *ApJ*, 668, 949
- Besla G., Kallivayalil N., Hernquist L., van der Marel R. P., Cox T. J., Kereš D., 2012, *MNRAS*, 421, 2109
- Besla G., Martínez-Delgado D., van der Marel R. P., Beletsky Y., Seibert M., Schlafly E. F., Grebel E. K., Neyer F., 2016, *ApJ*, 825, 20
- Bonaca A., Hogg D. W., 2018, *ApJ*, 867, 101
- Bonaca A., Hogg D. W., Price-Whelan A. M., Conroy C., 2018, arXiv e-prints, arXiv:1811.03631
- Bovy J., 2015, *ApJS*, 216, 29
- Bovy J., Erkal D., Sanders J. L., 2017, *MNRAS*, 466, 628
- Bowden A., Belokurov V., Evans N. W., 2015, *MNRAS*, 449, 1391
- Bowden A., Evans N. W., Belokurov V., 2013, *MNRAS*, 435, 928
- Cappellari M. et al., 2006, *MNRAS*, 366, 1126
- Carlberg R. G., 2009, *ApJ*, 705, L223
- Carlberg R. G., Grillmair C. J., 2013, *ApJ*, 768, 171
- Carlberg R. G., Grillmair C. J., Hetherington N., 2012, *ApJ*, 760, 75
- Choi Y. et al., 2018, *ApJ*, 869, 125
- de Boer T. J. L., Belokurov V., Koposov S. E., Ferrarese L., Erkal D., Côté P., Navarro J. F., 2018, *MNRAS*, 477, 1893
- Deason A. J., Belokurov V., Erkal D., Koposov S. E., Mackey D., 2017, *MNRAS*, 467, 2636
- Deason A. J., Belokurov V., Evans N. W., An J., 2012, *MNRAS*, 424, L44
- Debatista V. P., Roškar R., Valluri M., Quinn T., Moore B., Wadsley J., 2013, *MNRAS*, 434, 2971
- Dey A. et al., 2018, arXiv e-prints, arXiv:1804.08657
- Eadie G., Jurić M., 2018, arXiv e-prints, arXiv:1810.10036
- Erkal D., Belokurov V., 2015, *MNRAS*, 450, 1136
- Erkal D., Koposov S. E., Belokurov V., 2017, *MNRAS*, 470, 60
- Erkal D. et al., 2018, *MNRAS*, 481, 3148
- Erkal D., Sanders J. L., Belokurov V., 2016, *MNRAS*, 461, 1590
- Errani R., Peñarrubia J., Walker M. G., 2018, *MNRAS*, 481, 5073
- Evans N. W., 1994, *MNRAS*, 267, 333
- Fardal M. A., van der Marel R. P., Sohn S. T., del Pino Molina A., 2018, arXiv e-prints
- Fardal M. A. et al., 2013, *MNRAS*, 434, 2779
- Fellhauer M. et al., 2006, *ApJ*, 651, 167
- Foreman-Mackey D., Hogg D. W., Lang D., Goodman J., 2013, *PASP*, 125, 306
- Fritz T. K., Battaglia G., Pawlowski M. S., Kallivayalil N., van der Marel R., Sohn S. T., Brook C., Besla G., 2018, *A&A*, 619, A103
- Fritz T. K., Kallivayalil N., 2015, *ApJ*, 811, 123
- Gaia Collaboration et al., 2018, *A&A*, 616, A1
- Garavito-Camargo N., Besla G., Laporte C. F. P., Johnston K. V., Gómez F. A., Watkins L. L., 2019, arXiv e-prints
- Gibbons S. L. J., Belokurov V., Evans N. W., 2014, *MNRAS*, 445, 3788
- Gnedin O. Y., Brown W. R., Geller M. J., Kenyon S. J., 2010, *ApJ*, 720, L108
- Gnedin O. Y., Gould A., Miralda-Escudé J., Zentner A. R., 2005, *ApJ*, 634, 344
- Gómez F. A., Besla G., Carpintero D. D., Villalobos Á., O'Shea B. W., Bell E. F., 2015, *ApJ*, 802, 128
- Gómez F. A., White S. D. M., Marinacci F., Slater C. T., Grand R. J. J., Springel V., Pakmor R., 2016, *MNRAS*, 456, 2779
- Gravity Collaboration et al., 2018, *A&A*, 615, L15
- Grillmair C. J., 2006, *ApJ*, 645, L37
- Grillmair C. J., Dionatos O., 2006, *ApJ*, 643, L17
- Hayes C. R., Law D. R., Majewski S. R., 2018, *ApJ*, 867, L20
- Helmi A., 2004, *ApJ*, 610, L97
- Hendel D. et al., 2018, *MNRAS*, 479, 570
- Hernquist L., 1990, *ApJ*, 356, 359
- Hunter J. D., 2007, *Computing in Science Engineering*, 9, 90
- Ibata R., Chapman S., Ferguson A. M. N., Irwin M., Lewis G., McConnachie A., 2004, *MNRAS*, 351, 117
- Ibata R., Lewis G. F., Irwin M., Totten E., Quinn T., 2001, *ApJ*, 551, 294
- Ibata R. A., Lewis G. F., Irwin M. J., Quinn T., 2002, *MNRAS*, 332, 915
- Jethwa P., Erkal D., Belokurov V., 2016, *MNRAS*, 461, 2212
- Johnston K. V., Law D. R., Majewski S. R., 2005, *ApJ*, 619, 800
- Johnston K. V., Spergel D. N., Haydn C., 2002, *ApJ*, 570, 656
- Johnston K. V., Zhao H., Spergel D. N., Hernquist L., 1999, *ApJ*, 512, L109
- Jones E., Oliphant T., Peterson P., et al., 2001–, SciPy: Open source scientific tools for Python. <http://www.scipy.org/>
- Kallivayalil N. et al., 2018, *ApJ*, 867, 19
- Kallivayalil N., van der Marel R. P., Besla G., Anderson J., Alcock C., 2013, *ApJ*, 764, 161
- Kleyna J. T., Wilkinson M. I., Evans N. W., Gilmore G., 2005, *ApJ*, 630, L141
- Kochanek C. S., Keeton C. R., McLeod B. A., 2001, *ApJ*, 547, 50
- Koposov S. E. et al., 2019, *MNRAS*, 485, 4726
- Koposov S. E., Rix H.-W., Hogg D. W., 2010, *ApJ*, 712, 260
- Küpper A. H. W., Balbinot E., Bonaca A., Johnston K. V., Hogg D. W., Kroupa P., Santiago B. X., 2015, *ApJ*, 803, 80
- Laporte C. F. P., Gómez F. A., Besla G., Johnston K. V., Garavito-Camargo N., 2018, *MNRAS*, 473, 1218
- Law D. R., Majewski S. R., 2010, *ApJ*, 714, 229
- Levine E. S., Blitz L., Heiles C., 2006, *ApJ*, 643, 881
- Mackey A. D., Koposov S. E., Erkal D., Belokurov V., Da Costa G. S., Gómez F. A., 2016, *MNRAS*, 459, 239
- Mackey D., Koposov S., Da Costa G., Belokurov V., Erkal D., Kuzma P., 2018, *ApJ*, 858, L21
- Majewski S. R., Law D. R., Polak A. A., Patterson R. J., 2006, *ApJ*, 637, L25
- Malhan K., Ibata R. A., 2017, *MNRAS*, 471, 1005
- Malhan K., Ibata R. A., 2018, *MNRAS*, 477, 4063
- Mandelbaum R., Seljak U., Kauffmann G., Hirata C. M., Brinkmann J., 2006, *MNRAS*, 368, 715
- Miyamoto M., Nagai R., 1975, *PASJ*, 27, 533
- Moster B. P., Naab T., White S. D. M., 2013, *MNRAS*, 428, 3121
- Navarrete C. et al., 2019, *MNRAS*, 483, 4160
- Navarro J. F., Frenk C. S., White S. D. M., 1997, *ApJ*, 490, 493
- Newberg H. J., Willett B. A., Yanny B., Xu Y., 2010, *ApJ*, 711, 32
- Ngan W. H. W., Carlberg R. G., 2014, *ApJ*, 788, 181
- Nidever D. L. et al., 2019, *ApJ*, 874, 118
- Odenkirchen M. et al., 2001, *ApJ*, 548, L165
- Peñarrubia J., Gómez F. A., Besla G., Erkal D., Ma Y.-Z., 2016, *MNRAS*, 456, L54
- Pearson S., Küpper A. H. W., Johnston K. V., Price-Whelan A. M., 2015, *ApJ*, 799, 28
- Perez F., Granger B. E., 2007, *Computing in Science Engineering*, 9, 21
- Pietrzyński G. et al., 2013, *Nature*, 495, 76
- Price-Whelan A. M., Bonaca A., 2018, *ApJ*, 863, L20
- Price-Whelan A. M. et al., 2018, *AJ*, 156, 123
- Putman M. E., Staveley-Smith L., Freeman K. C., Gibson B. K., Barnes D. G., 2003, *ApJ*, 586, 170
- Reid M. J., Brunthaler A., 2004, *ApJ*, 616, 872
- Richstone D. O., 1980, *ApJ*, 238, 103
- Sales L. V., Navarro J. F., Cooper A. P., White S. D. M., Frenk C. S., Helmi A., 2011, *MNRAS*, 418, 648
- Sand D. J., Treu T., Ellis R. S., 2002, *ApJ*, 574, L129
- Sanders J. L., Binney J., 2013, *MNRAS*, 433, 1813
- Schommer R. A., Suntzeff N. B., Olszewski E. W., Harris H. C., 1992, *AJ*, 103, 447
- Schönrich R., Binney J., Dehnen W., 2010, *MNRAS*, 403, 1829
- Shipp N. et al., 2018, *ApJ*, 862, 114
- Siegal-Gaskins J. M., Valluri M., 2008, *ApJ*, 681, 80
- Simon J. D., 2018, *ApJ*, 863, 89
- Stanimirović S., Staveley-Smith L., Jones P. A., 2004, *ApJ*, 604, 176
- Treu T., Koopmans L. V. E., 2004, *ApJ*, 611, 739
- van der Marel R. P., 2006, in *The Local Group as an Astrophysical Laboratory*, Livio M., Brown T. M., eds., Vol. 17, pp. 47–71
- van der Marel R. P., Alves D. R., Hardy E., Suntzeff N. B., 2002, *AJ*, 124, 2639
- van der Marel R. P., Kallivayalil N., 2014, *ApJ*, 781, 121
- van der Walt S., Colbert S. C., Varoquaux G., 2011, *Computing in Science Engineering*, 13, 22

- Vasiliev E., 2019, MNRAS, 484, 2832
Vera-Ciro C., Helmi A., 2013, ApJ, 773, L4
Vesperini E., Weinberg M. D., 2000, ApJ, 534, 598
Walker M. G., Mateo M., Olszewski E. W., Peñarrubia J., Evans N. W., Gilmore G., 2009, ApJ, 704, 1274
Watkins L. L., Evans N. W., An J. H., 2010, MNRAS, 406, 264
Watkins L. L., van der Marel R. P., Sohn S. T., Evans N. W., 2018, arXiv e-prints, arXiv:1804.11348
Weinberg M. D., 1989, MNRAS, 239, 549
Weinberg M. D., 1998, MNRAS, 299, 499
Weinberg M. D., Blitz L., 2006, ApJ, 641, L33
White M., 2001, A&A, 367, 27
Wilkinson M. I., Evans N. W., 1999, MNRAS, 310, 645
Xue X. X. et al., 2008, ApJ, 684, 1143
Yoon J. H., Johnston K. V., Hogg D. W., 2011, ApJ, 731, 58
Zhu Q., Marinacci F., Maji M., Li Y., Springel V., Hernquist L., 2016, MNRAS, 458, 1559
Zivick P. et al., 2018, ApJ, 864, 55

APPENDIX A: BEST-FIT PARAMETERS

In this appendix, we give the best-fit (i.e maximum likelihood) parameters for each setup considered in Table 2.

Parameter	sph. MW+LMC	obl. MW+LMC	pro. MW+LMC	sph. rMW+LMC	obl. rMW+LMC	pro. rMW+LMC
Orphan						
$\mu_{\alpha, \text{prog}}^*$ (mas/yr)	-3.681	-3.779	-3.753	-3.653	-3.616	-3.796
$\mu_{\delta, \text{prog}}$ (mas/yr)	2.880	2.965	2.976	2.832	2.869	2.982
$v_{r, \text{prog}}$ (km/s)	107.573	111.877	105.708	97.055	111.716	97.590
d_{prog} (kpc)	18.764	17.889	18.057	18.350	17.833	17.846
$\phi_{2, \text{prog}}$ (°)	-0.441	-0.133	-0.657	-0.402	-0.857	-0.867
Milky Way						
$M_{\text{NFW}} (10^{10} M_{\odot})$	123.643	125.839	108.360	79.160	96.471	82.225
r_s (kpc)	17.707	21.244	18.902	12.807	19.550	15.013
q_{NFW}	–	0.898	1.227	–	0.851	1.272
l_{NFW} (°)	–	13.379	89.548	–	-39.448	94.759
b_{NFW} (°)	–	-3.736	29.556	–	9.001	29.145
LMC						
$M_{\text{LMC}} (10^{10} M_{\odot})$	7.173	10.464	8.391	12.501	9.038	12.657
$\mu_{\alpha, \text{LMC}}^*$ (mas/yr)	1.906	1.883	1.910	1.888	1.909	1.930
$\mu_{\delta, \text{LMC}}$ (mas/yr)	0.435	0.315	0.308	0.293	0.221	0.307
$v_{r, \text{LMC}}$ (km/s)	261.286	261.667	264.715	263.960	260.910	265.014
d_{LMC} (kpc)	48.009	50.537	50.999	47.893	49.241	52.184

Table A1. Best-fit values in the 6 setups from Tab. 2. For ease in reading, we give these in the same format as Tab. 1 where we described the priors.